Error Controlled Adaptive Multiscale Method For Fracture Modelling in Polycrystalline materials.

Ahmad Akbari Rahimabadi[a], Pierre Kerfriden [a,1,*], Stéphane Bordas[b]

[a] *Institute of Mechanics and Advanced Materials, Cardiff School of Engineering, Cardiff University, Cardiff,CF24 3AA, UK.*
[b] *Facult des Sciences, de la Technologie et de la Communication 6, University of Luxembourg, L-1359, Luxembourg*

Abstract

In this paper an adaptive multiscale method is presented in an attempt to address the lack of separation of scales in simulation of fracture. This method is set in the context of FE^2 [20] for which computational homogenisation breaks down upon loss of material stability (softening). The lack of scale separation due to the coalescence of microscopic cracks in a certain zone is tackled by a full discretisation of the microstructure in this zone. Polycrystalline materials are considered with cohesive cracks along the grain boundaries as a model problem. Adaptive mesh refinement of the coarse region and adaptive initiation and growth of fully resolved regions are performed based on discretisation error and homogenisation error criteria, respectively. In order to follow sharp snap-backs in load-displacement paths, a local arc-length technique is developed for the adaptive multiscale method. The results are validated against direct numerical simulation.

Keywords: Adaptive multiscale, nonlinear fracture mechanics, cohesive interface, adaptive mesh, homogenisation error, polycrystalline materials

Contents

1 Introduction **2**
1.1 Failure-oriented multiscale methods . . . 2
1.2 Proposed multiscale method . . . 4

2 microscopic structure **5**
2.1 Bulk Grain constitutive law . . . 6
2.2 Cohesive interface model for grain boundaries . . . 6
2.3 Finite Element Discretization . . . 10

3 Hybrid Multiscale Method **13**
3.1 Hierarchical Multiscale: FE^2 Method . . . 13
3.1.1 Homogenised constitutive law . . . 14
3.1.2 Limitations . . . 17
3.2 Macroscopic problem . . . 18
3.3 Concurrent Multiscale: Domain Decomposition Method . . . 20
3.4 Coupling Fine-Coarse meshes . . . 21
3.5 Solving the coupled problem . . . 22

4 Solution Procedure **24**
4.1 Error Estimation and Adaptive Mesh Refinement . . . 24
4.2 Homogenisation error . . . 25

*Corresponding author
[1] kerfridenp@cf.ac.uk

4.3 Zienkiewicz-Zhu error estimation . . . 27
4.4 Coarse mesh refinement procedure . . . 29
4.5 Adaptive expansion of fully resolved region . . . 30
4.6 Equalisation process . . . 31
4.7 Relaxation . . . 32

5 Local Arc-length technique **32**

6 Example Applications **36**
6.1 Notched Beam . . . 36

7 Conclusions **42**

1. Introduction

In many engineering designs, macroscale models cannot predict the behaviour of complex materials correctly [49, 17, 46]. Material failure, heterogeneous materials and multiphase problems may require more information than is available at the macroscale to construct constitutive relations and obtain material properties.
Multiscale modelling are aimed at solving problems for which macroscopic considerations are insufficient. For example, multiscale modelling is applicable to problems with complex material laws that fail to be determined by macroscopic approaches, or microscopic optimisation problems, where a bridge between micro and macro is required. Because of the large size of engineering structures, these problems cannot be solved completely at the micro-level, i.e. by resolving the micro structure explicitly on the whole domain of interest. Therefore it is reasonable to retain both the macroscopic and the microscopic points of view to find a practical technique to analyse such problems.

Most of the strategies for hierarchical multiscale modelling rely on homogenisation, which assumes a clear separation of scale. Hierarchical multiscale is basically an application of this principle using computational power to evaluate the homogenised properties ”on-the-fly”. Once the scale separation is lost, one must go lower in scale, which leads to hybrid multiscale solvers.
Hierarchical multiscale based on homogenisation fails to model the regions under high strain localisation due to the lack of scale separation assumption. However, in the case of fracture, these so called hierarchical multiscale methods cannot be used in the vicinity of cracks, as the separation of scales necessary for their application is lost.

1.1. Failure-oriented multiscale methods

In the literature, two techniques have been used in order to alleviate the absence of the scale separation assumption: i) Non-concurrent methods, ii) Concurrent methods.
The first scheme, the non-concurrent mutliscale, tries to extend the applicability of averaging techniques to fracture (e.g. [44, 3, 63, 50] for special averaging techniques dedicated to established damage bands). In fracture modelling, a macroscopic crack is represented by e.g. cohesive interface elements, and the associated constitutive model is derived from homogenisation. In these approaches, the classical homogenisation technique is modified to obtain a homogenised behaviour of the softening regime, while the microscopic model loses stability and the scale separation assumption ceases to exist. The principle of the modified homogenisation technique is based on a decomposition of the averaging procedure into two parts: one averaging over the region of the RVE where it is in the elastic regime and a second averaging over the region that is undergoing softening. This is a modified homogenisation to get the cohesive law of the macroscopic crack from the microstructure. Increasing the width of the RVE leads to a more brittle response because the RVE stores more elastic energy but dissipates a constant amount of energy due to the constant band of localisation. The idea is to filter out the elastic part so that the energy of the cohesive crack is equated

only to the energy of the part of the RVE that undergoes significant dissipation and damage localisation. In most of the existing approaches, the direction of propagation is found via macroscopic criteria, although some progresses have been achieved in the context of bottom up approach [11]. The latest work on the non-concurrent multiscale modeling of fracture can be found in [13, 51, 61, 60].

The second scheme, concurrent multiscale, makes use of a concurrent framework and attempt to detect the zone where the homogenisation fails directly at the microscale (e.g. [33, 62, 23, 41]). Although the latter approach is more general, it is " more costly" in terms of computation. Crack tip properties in a heterogeneous structure cannot be accurately determined by replacing the whole structure with a homogenised medium and calculating the SIF of the crack in that medium. For example, [65] proposed that the crack tip region must explicitly be retained with the actual microstructure, and at best replace the surrounding region with the homogenised medium.
The goal of concurrent multiscale fracture modelling is to take advantage of the fact that in fracture problems, only a small portion of the total domain is of interest [12]. To reach this goal, a concurrent multiscale scheme must establish a direct link between the macro and microscale without a prerequisite for scale separation. In this scheme, both scales (or all scales) are resolved simultaneously. Information is exchanged between the scales through their common interfaces. For crack propagation, the microscale domain needs to be adaptively expanded into the new critical regions [62, 41]. In a failure-oriented concurrent multiscale method, the main challenges are

- adequately modelling the coupling between the scales,
- determining those regions which must be modelled with a microscale and those for which a macroscale model is sufficient,

To tackle the first challenge of the failure-oriented concurrent multiscale method, several coupling techniques have been proposed in the literature in order to connect the macroscopic and the microscopic domains in a concurrent manner. These methods differ according to the physics of the problem. They include the arlequin method [16], mortar element method [7, 6], Linear multi-point connection (or the strong coupling) [41]. The latter will be employed in this thesis. [62] investigated three different coupling methods between coarse and fine scales: the mortar method which connects the fine mesh and coarse mesh through a non-overlapping interface in an average sense; the arlequin method which connects the two meshes through overlapping domains; and the strong coupling method which provides a strong non-overlapping connection between the displacement fields of the fine mesh and coarse mesh.
Different criteria have been employed to determine the scale of modelling in multiscale problems. These criteria can be either physically oriented (for example based on the level of stress, strain or damage [25, 41]) or mathematically oriented for example based on the macroscopic discretisation error inherent to the finite element approximation or the modelling error due to homogenised material properties [70, 24, 59, 64]). However, none of the failure-oriented multiscale methods have employed the modelling error as the scale adaptation criteria. In [52], both h- and p-adaptivity are used to reduce the discretisation error in the macroscopic computations, and same authors in [24] made use of the scale ratio criterion for transition between the scales. The scale ratio is the ratio of the characteristic length of the macroscopic elements to the size of the RVE.
[37] proposed a seamless scale-bridging technique that turns from a hierarchical multiscale strategy (classical homogenisation) to a concurrent multiscale strategy through a four-level procedure. In the first level, the size of the coarse element is much larger that the size of the RVE which means that the essential assumption of homogenisation is fulfilled, so the classical homogenisation is carried out (fully scale separation). In the second level, the size of the coarse element is slightly larger than the size of the RVE, then the local microscale problems are solved on Quadrature subscale Volume Elements (QSVE) as part of the integration scheme at the coarse scale (near-complete scale separation). In the third level, where the size of the coarse element is almost the same or slightly less than the size of the RVE, the microscale problem is solved on a Subscale Volume Element (SVE) that is identical to the coarse element (partial scale separation). Finally, if

the size of the coarse element is smaller than the size of the RVE, then there is no scale separation, and the problem is fully resolved at the fine scale. In their work, the coarse mesh was adaptively refined by an error estimator technique.
[59] studied the influence of microscopic heterogeneity, size of RVE, and macroscopic strain gradient on the first order homogenisation results. The homogenisation error is defined by comparing the results obtained form higher order homogenisation with those from the classical homogenisation. They shown that the strain sensitivity which is the macroscopic strain gradient times the length of RVE has the most influence on the accuracy of the first order homogenisation. They proposed a scale adaptation criterion based on the level of strain sensitivity of the coarse elements.
[64] proposed a concurrent adaptive multiscale method for elasticity which the error in the coarse scale discretization and the modelling error due to homogenisation are controlled.
According to this literature review, those concurrent multiscale methods that address the discretisation and homogenisation errors are not dealing with fracture and failure phenomena, e.g. [30, 24, 37, 59, 64]. The failure-oriented multiscale methods in the literature usually have a fixed macroscopic mesh without any control on the modelling or discretisation errors [62, 41, 58, 23].In this paper, a concurrent multiscale method will be presented that is designed to model crack propagation through an adaptive expansion of the microscopic region together with a mesh refinement procedure to control the both discretisation error at the coarse mesh and homogenisation error. The unstructured macroscopic mesh is an advantageous that allow us to model non-regular shapes.

1.2. Proposed multiscale method

In this work, we propose an adaptive hybrid multiscale method for modelling fracture in a heterogeneous material composed of orthotropic grains with cohesive interfaces between grains. Instead of a direct solver the FE^2 method, derived from the homogenisation technique, is employed to compute the effective behaviour of the heterogeneous microscopic medium at a much coarser scale in the non-critical region where the modelling error due to the homogenisation is still low. The coarse scale is discretised with non-structured triangular finite elements, and adaptive mesh refinement is used to control the discretization error. While the coarse mesh refinement retains the discretization error at a certain level, the modelling error increases due to the fact that the finer the coarse elements, the less the scale separation assumption is fulfilled, which is a key issue for homogenisation. The accuracy of homogenisation is examined by measuring the second gradient of displacement which is ignored in the first order homogenisation. A critical zone emerges when the second displacement gradient reaches the critical value, or if the underlying RVE (representative volume element of microstructure) of the element loses stability due to localisation. Thereafter, a zoom-in process is triggered to replace the corresponding coarse elements of the critical zone with a high resolution microscale mesh and gluing it to the coarse scale mesh through a strong coupling technique using Lagrange multipliers. The high resolution region can gradually be extended to the newly emerged critical zones. A local arc-length technique is adopted to control the opening of microscopic cohesive cracks.

In the next section 2, the microscale problem is defined. The constitutive model for a polycrystalline material will be given where the grains are modelled as linear elastic with cohesive interfaces. A thermodynamically consistent damage model is used for simulation of the cohesive interface between the grains.In Section 3, the hybrid multiscale method which is a combination of the hierarchical and concurrent multiscale methods will be introduced. The modelling of polycrystalline materials with the FE^2 method will be explained. Then, a non-overlapping domain decomposition method for non-conforming meshes will be detailed that allows us to model localisation in critical regions where the FE^2 method is not valid.In Section 4, the algorithmic aspect of the proposed adaptive multiscale method will be explained. In order to follow load-displacement paths, a robust local arc-length technique will be proposed. The coarse mesh refinement based on Zinkiewicz-Zhu error estimator will be discussed, and introduction of fully resolved microstructure in the critical regions based on homogenisation error [59] will be explained. Finally, in Section 6, a test case will

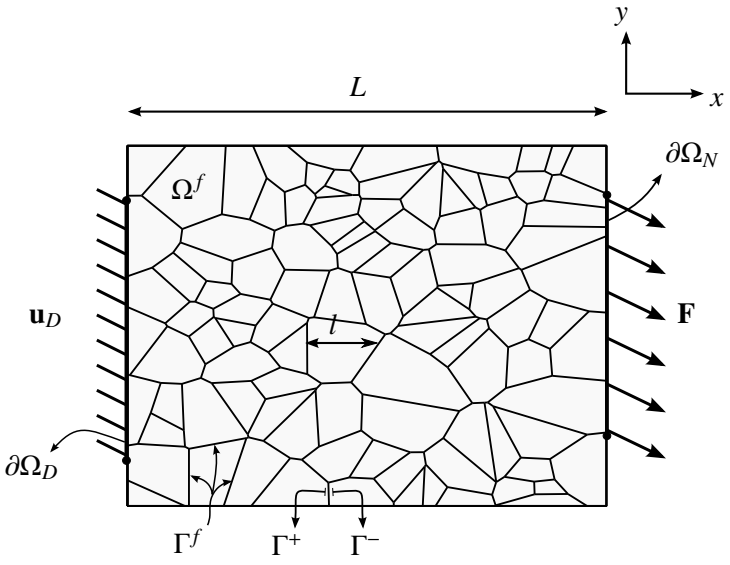

Figure 1: Microscale problem

be simulated with adaptive multiscale method and the results will be verified by direct numerical solution of the problems.

2. microscopic structure

Two-dimensional grains are modelled as linear elastic materials with cohesive interfaces between the grains. Only inter-granular fracture is considered, therefore cracks are not allowed to pass through the bulk grains. A thermodynamically consistent cohesive interface model is adopted to simulate inter-granular cracks. Figure 1 shows a domain Ω occupied by a structure consisting of randomly distributed orthotropic grains undergoing quasi-static small perturbations.

To start with, a boundary value problem of a structure where the polycrystalline material is represented explicitly is defined.

Given the displacement boundary condition $\mathbf{u}_D : \partial\Omega_D \rightarrow \mathbb{R}^2$ and the traction boundary condition $\mathbf{F} : \partial\Omega_N \rightarrow \mathbb{R}^2$, find $\mathbf{u}^f : \Omega \rightarrow \mathbb{R}^2$ such that, $\forall \delta\mathbf{u}^f \in \mathcal{U}_0$

$$\delta\Pi^f(\mathbf{u}^f, \delta\mathbf{u}^f) = \int_{\Omega^f \setminus \Gamma^f} \boldsymbol{\sigma}^f : \boldsymbol{\varepsilon}^f(\delta\mathbf{u}^f)\, \mathrm{d}\Omega + \int_{\Gamma^f} \mathbf{T}^f \cdot [\![\delta\mathbf{u}^f]\!]\, \mathrm{d}\Gamma - \int_{\partial\Omega_N} \mathbf{F} \cdot \delta\mathbf{u}^f\, \mathrm{d}\Gamma = 0 \tag{1}$$

$$(\boldsymbol{\sigma}^f \cdot \mathbf{n})\,|_{\mathbf{x}\in\Gamma^+} = -\,(\boldsymbol{\sigma}^f \cdot \mathbf{n})\,|_{\mathbf{x}\in\Gamma^-} = \mathbf{T}^f([\![\mathbf{u}^f]\!])\,|_{\mathbf{x}\in\Gamma^f}\ . \tag{2}$$

The superscript f indicate that the variables are at the fine scale. The vector $\mathbf{n}$ is a unit vector normal to the cohesive interface (see Fig. 6). $\delta\Pi^f$ is the virtual work, $\mathbf{u}^f \in \mathcal{U}$ is displacement field and $\delta\mathbf{u}^f \in \mathcal{U}_0$ is an arbitrary virtual displacement field. $\mathcal{U}$ and $\mathcal{U}_0$ are collection of trial,$\mathbf{u}^f$, and test functions,$\delta\mathbf{u}^f$ respectively, which can be defined by

$$\mathcal{U} = \{\mathbf{u} | \mathbf{u} \in H^1(\Omega^f \setminus \Gamma^f), \mathbf{u}|_{\partial\Omega_D} = \mathbf{u}_D\} \tag{3}$$

$$\mathcal{U}_0 = \{\delta\mathbf{u} | \delta\mathbf{u} \in H^1(\Omega^f \setminus \Gamma^f), \delta\mathbf{u}|_{\partial\Omega_D} = \mathbf{0}\} \tag{4}$$

where $H^1(\Omega^f \setminus \Gamma^f)$ is the Sobolev space of degree one for inside the grains not at the interfaces.

The Cauchy stress tensor, the strain tensor at the fine scale are $\boldsymbol{\sigma}^f$ and $\boldsymbol{\varepsilon}^f$, and the traction and displacement jump on the interfaces of grains, Γ^f, are denoted by $\mathbf{T}^f$ and $[\![\mathbf{u}^f]\!]$ respectively. Figure 6 displays the displacement jump $[\![\tilde{\mathbf{u}}]\!]$ as differences between the displacement of two slides of an interface. The microscopic grains are orthotropic material. The constitutive relationship for the grains is given by Hooke's law:

$$\boldsymbol{\sigma}^f_{|_{\mathbf{x},t}} = \mathbb{C}^f_{|_{\mathbf{x}}} : \boldsymbol{\varepsilon}^f(\mathbf{u}^f_{|_{\mathbf{x},t}}), \quad \text{in}\Omega^f \setminus \Gamma^f, \tag{5}$$

or in Voigt's form the constitutive equation is given by:

$$\boldsymbol{\sigma}^f_{|_{\mathbf{x},t}} = \mathbf{C}^f_{|_{\mathbf{x}}} \boldsymbol{\varepsilon}^f(\mathbf{u}^f_{|_{\mathbf{x},t}}), \quad \forall \mathbf{x} \in \Omega^f \setminus \Gamma^f, \tag{6}$$

where $\mathbb{C}^f$ is the fourth order stiffness tensor, and $\mathbf{C}^f$ is a matrix contains the constant elastic stiffness moduli of the grains. Note that the tensor form of stress and strain are shown by the same notation as used for their vector form since they can be distinguished in context. The constitutive relationship for the interface between grains is based on a cohesive interface model given by:

$$\delta\mathbf{T}^f(\mathbf{x}) = \mathbf{K}_{dT}\delta[\![\mathbf{u}^f(\mathbf{x})]\!], \quad \text{on } \Gamma^f, \tag{7}$$

where $\mathbf{K}_{dT}$ is the tangent stiffness matrix. In Section 2.2 the tangent stiffness matrix $\mathbf{K}_{dT}$ will be derived as a thermodynamically consistent function of the history of the displacement jump $[\![\mathbf{u}^f]\!]$ on the interface of the grains.

2.1. Bulk Grain constitutive law

The stiffness matrix for a 2D orthotropic grain, used in constitutive equation (6), can be written in Voigt form:

$$\tilde{\mathbf{C}}^f = \begin{bmatrix} C_{11} & C_{12} & 0 \\ C_{21} & C_{22} & 0 \\ 0 & 0 & C_{66} \end{bmatrix}, \tag{8}$$

where C_{ij} are elastic constants and and $C_{12} = C_{21}$. The subscripts 1 and 2 refer to the material principal coordinates (see Fig. 2). To obtain the stiffness matrix in the global coordinate system, the following matrix transformation is employed:

$$\mathbf{C}^f = \mathbf{T}_\sigma^{-1}\tilde{\mathbf{C}}^f\mathbf{T}_\varepsilon \tag{9}$$

where the transformation matrices are given by

$$\mathbf{T}_\varepsilon^T = \mathbf{T}_\sigma^{-1} = \begin{bmatrix} \cos^2\theta & \sin^2\theta & -\sin 2\theta \\ \sin^2\theta & \cos^2\theta & \sin 2\theta \\ 0.5\sin 2\theta & -0.5\sin 2\theta & \cos 2\theta \end{bmatrix}, \tag{10}$$

Figure 2 illustrates θ, which is the angle between the material coordinate system, $(1, 2)$, and the global coordinate system, (x, y).

2.2. Cohesive interface model for grain boundaries

The potential failure of the interface between adjacent grains is described by a thermodynamically consistent cohesive model in the local coordinate system $(\tilde{x}, \tilde{y})$ (see Fig. 2 and 6). A material point at the cohesive interfaces is considered as the thermodynamic system. The variation of temperature and heat conduction are neglected due to isothermal and homogeneous temperature assumptions, respectively.
The free energy function for an isotropic damage is defined by [39]:

$$\Psi([\![\tilde{\mathbf{u}}]\!], d) = \phi(d)\Psi_0([\![\tilde{\mathbf{u}}]\!]). \tag{11}$$

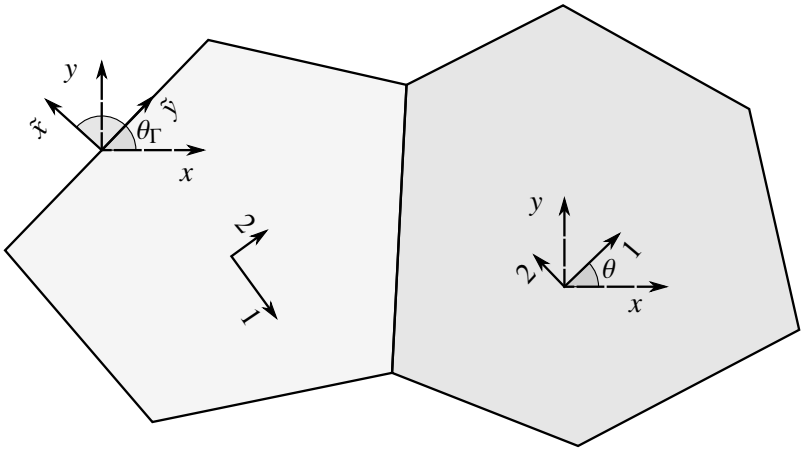

Figure 2: Local coordinates on the boundary of a grain $(\tilde{x}, \tilde{y})$, Local coordinates on the principal direction of the orthotropic grain $(1, 2)$, and global coordinate (x, y).

The damage function is usually chosen as $\phi(d) = 1 - d$, where $d \in [0, 1]$ indicates the level of damage in the interface. Ψ_0 is the energy for an undamaged elastic interface that is defined by $\Psi_0 = 0.5[\![\tilde{\mathbf{u}}]\!]^T \tilde{\mathbf{K}}_0 [\![\tilde{\mathbf{u}}]\!]$, where $\tilde{\mathbf{K}}_0$ is the original (initial) stiffness of the interface. The traction-separation law for any arbitrary point at the cohesive interfaces are given by:

$$\tilde{\mathbf{T}} = \frac{\partial \Psi([\![\tilde{\mathbf{u}}]\!], d)}{\partial [\![\tilde{\mathbf{u}}]\!]} = \phi(d) \frac{\partial \Psi_0([\![\tilde{\mathbf{u}}]\!])}{\partial [\![\tilde{\mathbf{u}}]\!]} = (1 - d)\tilde{\mathbf{K}}_0 [\![\tilde{\mathbf{u}}]\!], \tag{12}$$

This equation is valid for opening crack. Now, it is required to evaluate the damage parameter d. In order to fulfil the second law of thermodynamics, the damage parameter d must increase monotonically. We choose a power-law damage evolution for our model [48]:

$$d(\kappa) = \begin{cases} 0 & \kappa < \kappa_{\text{ini}} \\ 1 - \left(\frac{\kappa_{\text{ful}} - \kappa}{\kappa_{\text{ful}} - \kappa_{\text{ini}}}\right)^n & \kappa_{\text{ini}} < \kappa < \kappa_{\text{ful}} \\ 1 & \kappa > \kappa_{\text{ful}} \end{cases} \tag{13}$$

where n is a material variable. κ_{ini} and κ_{ful} are the thresholds of the internal variable κ that are associated with the initiation and the fully damaged conditions of the interface crack respectively. For time $t + \Delta t$, κ is given by:

$$\kappa(t + \Delta t) = \max\left(\kappa(t); u_{\text{eff}}\right), \quad u_{\text{eff}} = \left\| \begin{array}{c} [\![\tilde{u}_n]\!] \mathcal{H}([\![\tilde{u}_n]\!]) \\ [\![\tilde{u}_t]\!] \end{array} \right\|, \tag{14}$$

where $\| \cdot \|$ is $L2$ norm, $[\![\tilde{u}_n]\!]$ and $[\![\tilde{u}_t]\!]$ are the normal and tangential component of the displacement jump $[\![\tilde{\mathbf{u}}]\!]$. The function 'max' does not allow κ to decrease, and the Heaviside function $\mathcal{H}([\![\tilde{u}_n]\!])$ prevents the negative jump in normal direction $[\![\tilde{u}_n]\!] < 0$ (associated with compression mode) from having an influence on the damage variable. Figure 3 shows a schematic profile for the damage parameter d. Due to a lack of precise knowledge, we assume that the critical fracture energy of modes I and II and the maximum tensile and shear strengths are equal ($G_{Ic} = G_{IIc}$ and $\sigma_{\max} = \tau_{\max}$). The internal variable threshold κ_{ini} assumed to be zero. The parameters introduced in the damage evolution law, Eq. (13), can be evaluated by the following equations:

$$G_{Ic} = \int_0^{[\![u]\!]_{\text{full}}} \tilde{T}_n \, \mathrm{d}[\![\tilde{u}_n]\!], \tag{15}$$

$$\sigma_{\max} = \left\{ \tilde{T}_n([\![\tilde{u}_n]\!]) \,\middle|\, \frac{\mathrm{d}\tilde{T}_n}{\mathrm{d}[\![\tilde{u}_n]\!]} = 0 \right\}. \tag{16}$$

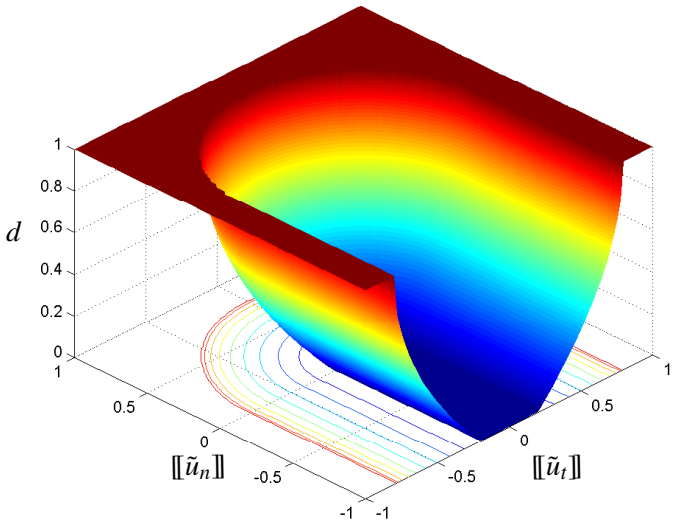

Figure 3: A schematic illustration of a damage evolution function based on Eqs. (13) and (14). In this figure, $\kappa_{\text{ini}} = 0.2$, $\kappa_{\text{full}} = 0.8$ and $n = 0.5$.

Equation (15) states that the fracture energy equals to the total work of external load that leads to a fully opened cohesive interface ($[\![\tilde{u}_n]\!] = [\![u]\!]_{\text{full}}$), and Eq. (16) states that the maximum normal stress occurs at the stationary point of the traction-separation law. In order to follow the loading path of the traction-separation curve, it is assumed that the normal jump along the interface monotonically increases. Thus we are allowed to use the normal jump directly in the equation of damage evolution (13). Finally by solving Eq. (15) and (16) we find that:

$$\kappa_{\text{full}} = [\![u]\!]_{\text{full}} = \alpha \frac{G_{Ic}}{\sigma_{\max}}, \quad \alpha = (n+2)\left(\frac{n}{n+1}\right)^n \tag{17}$$

$$k_n = k_t = \beta \frac{\sigma_{\max}^2}{G_{Ic}}, \quad \beta = \frac{(n+1)}{(n+2)}\left(\frac{n+1}{n}\right)^{2n} \tag{18}$$

where the original stiffness of cohesive interface in normal and tangential directions, k_n and k_t, are assumed to be equal. The variations of α and β versus n are shown in Fig. 4. β is limited to $\beta \in (0, \exp(2))$, which means the stiffness coefficients are bound between $0.5\frac{\sigma_{\max}^2}{G_{Ic}} < k_n = k_t < \exp(2)\frac{\sigma_{\max}^2}{G_{Ic}}$. In the rest of the paper $n = 0.5$, and consequently, $k_n = k_t =$. The influence of n on the traction-separation law and overall response of structure still needs to be studied, however this is beyond the scope of this work, where we assume that a material model is available and develop general tools able to rely on advances in such material models.
Inspired by [4], the traction-separation relationship and the stiffness matrix of the cohesive interface is modified to give a non-damageable stiffness in compression loading:

$$\tilde{\mathbf{T}} = \tilde{\mathbf{K}}_d [\![\tilde{\mathbf{u}}^f]\!] \quad \text{where} \quad \tilde{\mathbf{K}}_d = \begin{bmatrix} k_n^+ (1-d)\,\mathcal{H}([\![\tilde{u}_n^f]\!]) + k_n^- \mathcal{H}(-[\![\tilde{u}_n^f]\!]) & 0 \\ 0 & k_t(1-d) \end{bmatrix}. \tag{19}$$

The subscript t refers to the tangential direction of the interface and n refers to the normal to the interface (See Fig. 6). k_t and k_n are original interface stiffness with dimension of force over length cubed. In order to avoid the penetration of grains into each other, the original interface stiffness for the closing mode is chosen to be much larger than the original interface stiffness for the opening mode, $k_n^-/k_n^+ > 1$. It is noted that a very

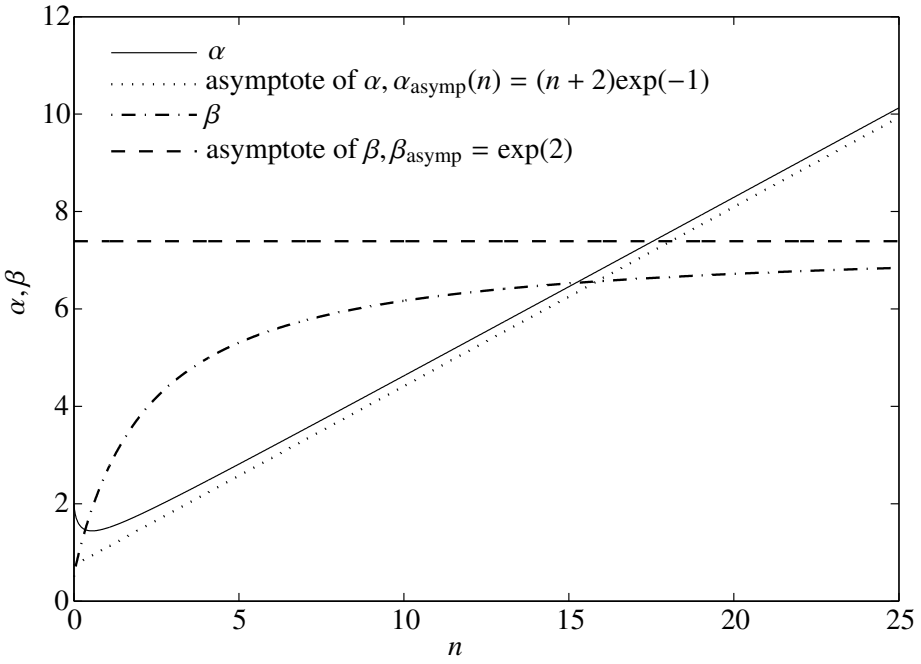

Figure 4: Variation of α and β versus n (see Eqs. (17) and (18)). Different choice of n can affect the original stiffness of cohesive cracks ($k_n \propto \beta$) and the required jump for a fully damaged crack ($[\![\mathbf{u}^f]\!]_{\text{full}} \propto \alpha$).

large value of k_n^- causes ill-conditioning of the stiffness matrix in finite element procedure. In this study, $k_n^-/k_n^+ = 100$. The Heaviside function $\mathcal{H}$ does not allow the damage parameter to influence the stiffness of the cohesive crack in compression mode. Figure 5 shows the traction-separation law for a one-dimension cohesive interface.

The tangent stiffness of a cohesive element is required for Newton-Raphson iterative solver

$$\begin{aligned}\tilde{\mathbf{K}}_{dT} &= \frac{\mathrm{d}\tilde{\mathbf{T}}}{\mathrm{d}[\![\tilde{\mathbf{u}}^f]\!]} = \frac{\partial\tilde{\mathbf{T}}}{\partial[\![\tilde{\mathbf{u}}^f]\!]} + \frac{\partial\tilde{\mathbf{T}}}{\partial d}\frac{\partial d}{\partial[\![\tilde{\mathbf{u}}^f]\!]} \\ &= \tilde{\mathbf{K}}_d - \frac{1}{\kappa}\frac{\partial d}{\partial\kappa}\begin{bmatrix} k_n^+\mathcal{H}([\![\tilde{u}_n^f]\!]) & 0 \\ 0 & k_t \end{bmatrix}\begin{Bmatrix} [\![\tilde{u}_n^f]\!] \\ [\![\tilde{u}_t^f]\!] \end{Bmatrix}\Big[[\![\tilde{u}_n^f]\!]\mathcal{H}([\![\tilde{u}_n^f]\!])\,,\ [\![\tilde{u}_t^f]\!]\Big], \quad \forall\kappa > 0\end{aligned} \tag{20}$$

In the case $\kappa = 0$ then $\tilde{\mathbf{K}}_{dT} = \tilde{\mathbf{K}}_d$.

The constitutive equation of cohesive interface in the global coordinate system is obtained by using the transformation matrix, $\mathbf{T}_\Gamma$:

$$\mathbf{T} = \mathbf{T}_\Gamma^{-1}\tilde{\mathbf{K}}_d\mathbf{T}_\Gamma[\![\mathbf{u}^f]\!] \quad \text{where} \quad \mathbf{T}_\Gamma = \begin{bmatrix} \cos\theta_\Gamma & -\sin\theta_\Gamma \\ \sin\theta_\Gamma & \cos\theta_\Gamma \end{bmatrix}. \tag{21}$$

θ_Γ is the angle between the global coordinate system and the local coordinate system on the boundary of the grains which is shown in Fig. 2.

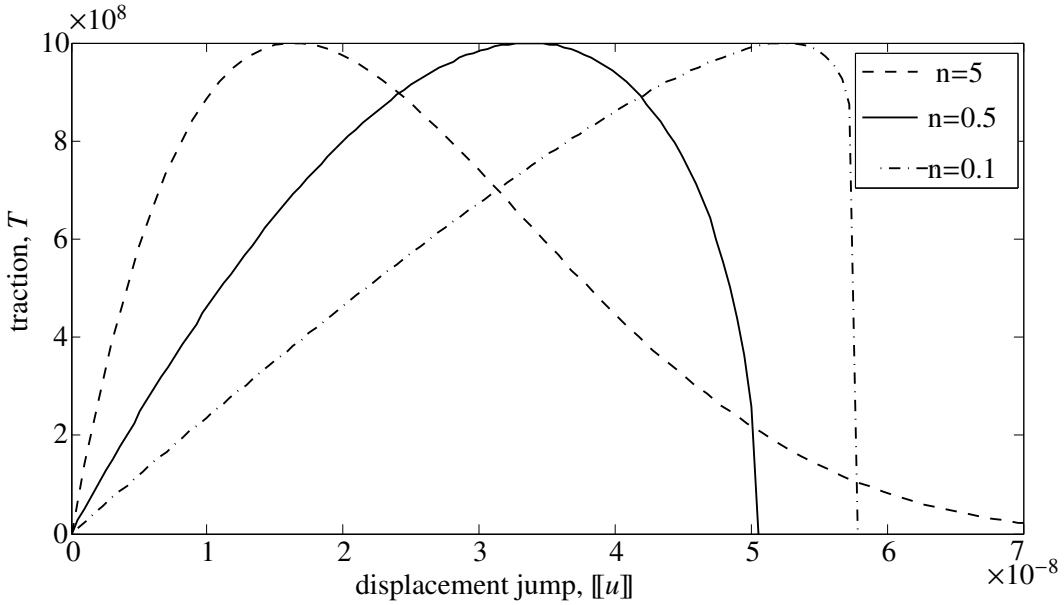

Figure 5: Traction-displacement curve for different value of parameter n in one dimension cohesive interface. In this figure, $\kappa_{ini} = 0$, the critical fracture energy equals $G_{Ic} = 35\frac{J}{m^2}$ and the maximum tensile strength is $\sigma_{\max} = 1$GPa [56].

2.3. Finite Element Discretization

In order to use Eq. (1) in the finite element method, first it is changed this equation to the Voigt notation. Recalling that the tensor and voight notations are the same:

$$\delta\Pi^f = \int_{\Omega^f \setminus \Gamma^f} \delta\boldsymbol{\varepsilon}^{f\,T} \boldsymbol{\sigma}^f \, \mathrm{d}\Omega + \int_{\Gamma^f} [\![\delta \mathbf{u}^f]\!]^T \mathbf{T}^f \, \mathrm{d}\Gamma - \int_{\partial\Omega_N} \delta\mathbf{u}^{f\,T} \mathbf{F} \, \mathrm{d}\Gamma = 0. \tag{22}$$

where $\delta\boldsymbol{\varepsilon}^f$ and $\boldsymbol{\sigma}^f$ are the vector form of virtual strain and stress tensor respectively:

$$\delta\boldsymbol{\varepsilon}^{f\,T} = \left[\frac{\partial \delta u^f}{\partial x} \quad \frac{\partial \delta v^f}{\partial y} \quad \left(\frac{\partial \delta u^f}{\partial y} + \frac{\partial \delta v^f}{\partial x} \right) \right], \tag{23}$$

$$\boldsymbol{\sigma}^f = \left[\sigma^f_{xx} \;\; \sigma^f_{yy} \;\; \sigma^f_{xy} \right]^T. \tag{24}$$

The FE formulation is developed by discretising Eq. (22) spatially. The orthotropic grains discretised by linear triangular finite elements.The interface of grains is discretized by 4-node cohesive elements with two integration points (see Fig. 6). The approximation of the displacement field $\mathbf{u}^f$ and strain $\boldsymbol{\varepsilon}^f$ in element (e) are given by:

$$\forall \mathbf{x} \in \Omega^f_e, \quad \mathbf{u}^f(\mathbf{x}) = \mathbf{N}_e \mathbf{U}^f_e, \tag{25}$$

$$\forall \mathbf{x} \in \Omega^f_e, \quad \boldsymbol{\varepsilon}^f(\mathbf{x}) = \mathbf{B}_e \mathbf{U}^f_e, \tag{26}$$

$$\tag{27}$$

where $\mathbf{N}_e$ is the linear shape function matrix, $\mathbf{B}_e$ is the matrix of the shape functions derivatives, and $\mathbf{U}^f$ is

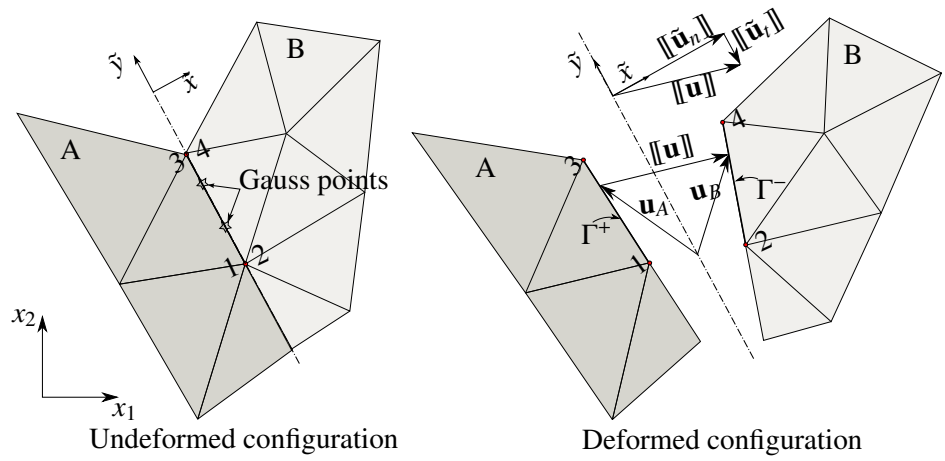

Figure 6: Local coordinate system on the boundary of a grain, $(\tilde{x}, \tilde{y})$, and displacement jump, $[\![\mathbf{u}]\!]$ in the local coordinate system. It is noted that the translation and rotation of local coordinates due to deformation can be neglected since small deformation is assumed. The node arrangement in the cohesive element must be based on the following construction: a) Node 1 and Node 3 belong to one grain, and Node 2 and Node 4 belong to the other grain, b) Node 1 has same position of Node 2, and Node 3 has the same position of Node 4, c) Nodes 1 and 3 must be chosen so that their grain fallen in the left side of the path from Node 1 to Node 3, d) The unit vectors of the local coordinate system are given by $\hat{\mathbf{t}} = \dfrac{\mathbf{x}_3 - \mathbf{x}_1}{\|\mathbf{x}_3 - \mathbf{x}_1\|}$ and $\hat{\mathbf{n}} = [\hat{t}_x\ ,\ -\hat{t}_y]^T$, e) Therefore the displacement jump is defined by: $[\![\mathbf{u}^f(\tilde{y})]\!] = \mathbf{u}^f_B(\tilde{y}) - \mathbf{u}^f_A(\tilde{y})$.

the nodal displacement vector:

$$\mathbf{N}_e(\mathbf{x}) = \begin{bmatrix} N_1(\mathbf{x}) & 0 & N_2(\mathbf{x}) & 0 & N_3(\mathbf{x}) & 0 \\ 0 & N_1(\mathbf{x}) & 0 & N_2(\mathbf{x}) & 0 & N_3(\mathbf{x}) \end{bmatrix}_e, \tag{28}$$

$$\mathbf{B}_e(\mathbf{x}) = \begin{bmatrix} \frac{\partial N_1}{\partial x} & 0 & \frac{\partial N_2}{\partial x} & 0 & \frac{\partial N_3}{\partial x} & 0 \\ 0 & \frac{\partial N_1}{\partial y} & 0 & \frac{\partial N_2}{\partial y} & 0 & \frac{\partial N_3}{\partial y} \\ \frac{\partial N_1}{\partial y} & \frac{\partial N_1}{\partial x} & \frac{\partial N_2}{\partial y} & \frac{\partial N_2}{\partial x} & \frac{\partial N_3}{\partial y} & \frac{\partial N_3}{\partial x} \end{bmatrix}_e \tag{29}$$

$$\mathbf{U}_e^{fT} = \begin{bmatrix} U_1^f & V_1^f & U_2^f & V_2^f & U_3^f & V_3^f \end{bmatrix}_e. \tag{30}$$

where U_i^f and V_i^f are the the displacement of node i in x- and y-directions respectively. The displacement jump $[\![\mathbf{u}^f]\!]$ in the cohesive elements (d) can be obtained by defining a matrix that contains the linear shape functions:

$$\forall \mathbf{x} \in \Gamma_d^f \quad [\![\mathbf{u}^f]\!](\mathbf{x}) = \mathbf{B}_d(\mathbf{x})^\Gamma \mathbf{U}_d^f, \tag{31}$$

$$\mathbf{B}_d^\Gamma(\mathbf{x}) = \begin{bmatrix} -N_1 & 0 & N_2 & 0 & -N_3 & 0 & N_4 & 0 \\ 0 & -N_1 & 0 & N_2 & 0 & -N_3 & 0 & N_4 \end{bmatrix}_d, \tag{32}$$

$$\mathbf{U}_d^f = \begin{bmatrix} U_1 & V_1 & U_2 & V_2 & U_3 & V_3 & U_4 & V_4 \end{bmatrix}_d^T. \tag{33}$$

where Γ_d^f is the interface between the grains, and the shape functions of cohesive elements are the trace of the shape functions on the adjacent triangular elements. It is noted that the jump extractor matrix $\mathbf{B}_d^f$ is designed based on the particular node arrangement that have been explained in Fig. 6.

Finally, finite element discretization of Eq. (22) writes:

$$\delta\Pi^f(\mathbf{U}^f, \delta\mathbf{U}^f) = \delta\mathbf{U}^{fT}\left(\sum_{e=1}^{n_B}\mathbf{M}_e\int_{\Omega_e^f\setminus\Gamma^f}\mathbf{B}_e^{fT}\boldsymbol{\sigma}_e^f\,\mathrm{d}\Omega + \sum_{d=1}^{n_C}\bar{\mathbf{M}}_d\int_{\Gamma_d^f}\mathbf{B}_d^{\Gamma T}\mathbf{T}_d^f\,\mathrm{d}\Gamma - \sum_{e=1}^{n_B}\mathbf{M}_e\int_{\partial\Omega_N}\mathbf{N}_e{}^T\mathbf{F}\,\mathrm{d}\Gamma\right) = 0. \tag{34}$$

where $\mathbf{M}_e$ and $\bar{\mathbf{M}}_d$ are the boolean matrices that maps respectively the bulk element and the cohesive element vectors to the corresponding entries of global vectors. The total number of triangular elements and cohesive elements are n_B and n_C respectively. Since the variational work is zero for any admissible variation of displacement vector $\delta\mathbf{U}^f$, it is concluded that the residual force vector must be null:

$$\mathbf{R}^f\left(\mathbf{U}^f\right) = \mathbf{f}_{\text{int}}\left(\mathbf{U}^f\right) - \mathbf{f}_{\text{ext}} = \mathbf{0}, \tag{35}$$

$$\mathbf{f}_{\text{int}}\left(\mathbf{U}^f\right) = \sum_{e=1}^{n_B}\mathbf{M}_e\int_{\Omega_e^f\setminus\Gamma^f}\mathbf{B}_e^{fT}\boldsymbol{\sigma}_e^f\,\mathrm{d}\Omega + \sum_{d=1}^{n_C}\bar{\mathbf{M}}_d\int_{\Gamma_d^f}\mathbf{B}_d^{\Gamma T}\mathbf{T}_d^f\,\mathrm{d}\Gamma \tag{36}$$

$$\mathbf{f}_{\text{ext}} = \sum_{e=1}^{n_B}\mathbf{M}_e\int_{\partial\Omega_N}\mathbf{N}_e{}^T\mathbf{F}\,\mathrm{d}\Gamma. \tag{37}$$

Because of the nonlinear behaviour of the cohesive interface elements, Eq. (35) cannot be solved directly for $\mathbf{U}^f$. The Newton-Raphson procedure is employed to find the solution iteratively. Therefore, Eq. (35) is linearised with respect to the displacement vector $\mathbf{U}^f$:

$$\begin{aligned}\bar{\mathbf{R}}^f\left(\mathbf{U}^f + \Delta\mathbf{U}^f\right) &\approx \mathbf{R}^f(\mathbf{U}^f) + \frac{\partial\mathbf{R}^f\left(\mathbf{U}^f\right)}{\partial\mathbf{U}^f}\Delta\mathbf{U}^f \\ &= \mathbf{f}_{\text{int}}\left(\mathbf{U}^f\right) - \mathbf{f}_{\text{ext}} + \frac{\partial\mathbf{f}_{\text{int}}^f\left(\mathbf{U}^f\right)}{\partial\mathbf{U}^f}\Delta\mathbf{U}^f.\end{aligned} \tag{38}$$

In the linearised equilibrium equation (38) the term $\dfrac{\partial\mathbf{f}_{\text{int}}^f\left(\mathbf{U}^f\right)}{\partial\mathbf{U}^f}$ is the tangent stiffness matrix $\mathbf{K}_T^f$ that is given by:

$$\frac{\partial\mathbf{f}_{\text{int}}^f\left(\mathbf{U}^f\right)}{\partial\mathbf{U}^f} = \sum_{e=1}^{n_B}\mathbf{M}_e\left(\int_{\Omega_e^f\setminus\Gamma^f}\mathbf{B}_e^{fT}\frac{\partial\boldsymbol{\sigma}_e^f}{\partial\mathbf{U}_e^f}\,\mathrm{d}\Omega\right)\mathbf{M}_e^T + \sum_{d=1}^{n_C}\bar{\mathbf{M}}_d\left(\int_{\Gamma_d^f}\mathbf{B}_d^{\Gamma T}\frac{\partial\mathbf{T}_d^f}{\partial\mathbf{U}_d^f}\,\mathrm{d}\Gamma\right)\bar{\mathbf{M}}_d^T \tag{39}$$

where

$$\frac{\partial\boldsymbol{\sigma}_e^f}{\partial\mathbf{U}_e^f} = \frac{\partial\boldsymbol{\sigma}_e^f}{\partial\boldsymbol{\varepsilon}_e^f}\frac{\partial\boldsymbol{\varepsilon}_e^f}{\partial\mathbf{U}_e^f} = \mathbf{C}_e^f\mathbf{B}_e^f, \tag{40}$$

$$\frac{\partial\mathbf{T}_d^f}{\partial\mathbf{U}_d^f} = \frac{\partial\mathbf{T}_d^f}{\partial[\![\mathbf{u}^f]\!]_d}\frac{\partial[\![\mathbf{u}^f]\!]_d}{\partial\mathbf{U}_d^f} = \mathbf{K}_{dT_d}\mathbf{B}_d^\Gamma. \tag{41}$$

where $\mathbf{C}^f$ is the stiffness matrix of the bulk element e given by Eq. 9, and $\mathbf{K}_{dT}$ is the stiffness matrix of the interface element d given by Eq. 21. Then, the tangent stiffness matrix can be written as following:

$$\mathbf{K}_T^f = \sum_{e=1}^{n_B}\mathbf{M}_e\left(\int_{\Omega_e^f\setminus\Gamma^f}\mathbf{B}_e{}^T\mathbf{C}_e^f\mathbf{B}_e\,\mathrm{d}\Omega\right)\mathbf{M}_e^T + \sum_{d=1}^{n_C}\bar{\mathbf{M}}_d\left(\int_{\Gamma_d^f}\mathbf{B}_d^{\Gamma T}\mathbf{K}_{dT_d}\mathbf{B}_d^\Gamma\,\mathrm{d}\Gamma\right)\bar{\mathbf{M}}_d^T, \tag{42}$$

Finally, by assuming $\bar{\mathbf{R}}^f\left(\mathbf{U}^f + \Delta\mathbf{U}^f\right) = \mathbf{0}$, the variation of the displacement at each iteration of the Newton-

Raphson solver is obtained by:

$$\Delta \mathbf{U}^f = \mathbf{K}_T^{f^{-1}} \mathbf{R}^f(\mathbf{U}^f). \tag{43}$$

In this section, a constitutive model for the polycrystalline microstructure was introduced. A two-dimensional orthotropic constitutive model is considered for the bulk grains. The interfaces of the grains are modelled with a thermodynamically consistent damage model and the underlying damage evolution law were explained. Since the modelling of engineering problems in the grain level is not affordable, a multiscale method is developed that make it possible to model the engineering problem by considering microscopic scale. In the next section, two classes of multiscale methods which are the base of the proposed multiscale technique will be introduced.

3. Hybrid Multiscale Method

This section explains a hierarchical multiscale method, based on computational homogenisation, combined with a concurrent multiscale method, based on domain decomposition. Homogenisation and domain decomposition are two bases for a broad range of multiscale methods in solid and fracture mechanics. A hybrid multiscale method can employ the advantages of both technique. Homogenisation techniques, known as hierarchical methods, aim at obtaining the average quantities of the constitutive relation for a macroscopic point by testing at a spatial sample of the heterogeneous microstructure which is called a Representative Volume Element (RVE). In computational homogenisation methods, the constitutive equations do not need to be explicitly defined at the macro-level. Incremental macroscopic stress-strain laws are obtained on-the-fly during the macroscopic solution process by solving the boundary value problem associated with the RVE at each (quadrature) point of the macroscopic problem. The boundary conditions of the RVE are defined by macroscopic state variables, e.g., strain or stress. The overall response of the RVE is used to determine the macroscopic constitutive equation [57, 20, 34]. As explained in introduction, an RVE cannot be found for the softening regime, and therefore, the homogenisation technique cannot be employed in the area with the strain localisation.
Domain decomposition method is well suited to the solution of fracture problems in a multiscale framework, in which the domain is split naturally into fine scale regions and coarse scale regions. The fine scale in the area of strain localisation with a fine discretisation is glued to the surrounding coarse mesh through overlapping or non-overlapping coupling methods, and the global solution is obtained by solving fine and coarse meshes concurrently. For our problem, domain decomposition method is used to model fracture in polycrystalline materials by splitting the domain into the microscopic sub-domain and macroscopic sub-domain, which microscopic domain composed of grains with cohesive cracks while the macroscopic sub-domain is a homogeneous domain.

3.1. Hierarchical Multiscale: FE^2 Method

In this section, a hierarchical multiscale method based on computational homogenisation for a nonlinear heterogeneous material (the fracture of polycrystalline materials) is detailed. In this method the effective material properties are computed by using averaging theorems applied to kinematic and static quantities of the heterogeneous microscale material. This method is based on the scale separation assumption, which requires, 1) the gradient of the macroscopic fields are not extensive over the underlying microstructure, and 2) the fluctuation of the microscopic fields affect the macroscopic behaviour only through their volume average [8]. Homogenisation provides a bridge between scales by mapping the average of the stress from the microscale to the macroscale and downscaling the macroscopic deformation tensor to the boundary of the microscopic RVE. The main advantages of computational homogenisation technique are:

- Computational homogenisation is a general method, even for very nonlinear problems as opposed to semi-analytical methods, e.g. mean-fields, that require some homogeneity of the micro fields in each micro phase.
- It does not require for explicit macroscopic constitutive law trough heuristic curve-fitting.

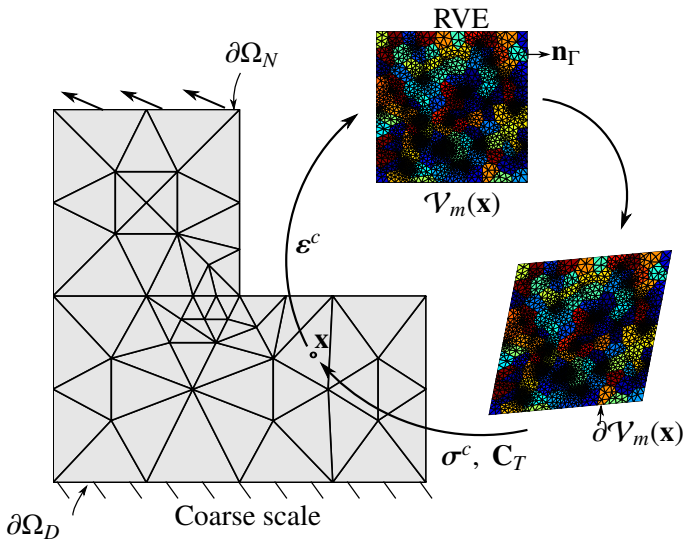

Figure 7: FE^2 scheme

- In comparison with semi-analytical mean-field theories, computational homogenisation method potentially is more accurate since there is no approximation of the fields in its underlying RVE.
- It gives useful insight in micro-fields due to the previous point.

In homogenisation method, the macroscopic deformation tensor provides the boundary conditions for the microscopic RVE. The solution of the boundary value problem for the RVE yields the tangent stiffness moduli and the macroscopic stress tensor which can then be used for calculating the internal force vector at the macroscale. This hierarchical multiscale method that implicitly defines nonlinear homogenised constitutive relationships is often called the FE^2 method [20] since the finite element method is used at both the macro and micro scales.

3.1.1. Homogenised constitutive law

The coarse scale constitutive law (69) at an arbitrary point $\mathbf{x}$ is obtained through homogenisation. The material point $\mathbf{x}$ can be related to a representative volume element (RVE). The RVE, $\mathcal{V}_\diamond(\mathbf{x})$, must statistically represents the heterogeneity of the microstructure in the vicinity of the corresponding macroscopic point $\mathbf{x}$. The relation between $\boldsymbol{\sigma}^c$ and $\boldsymbol{\varepsilon}^c$ is obtained by solving a boundary-value problem over the RVE. The volume average of properties over the RVE is used at the corresponding point $\mathbf{x}$ at the coarse scale, Fig. 7.
According to homogenisation, the macroscopic strain, stress, and strain energy at a local point, $\mathbf{x}$, are respectively related to the volume average of the strain and stress fields, and the strain energy of corresponding microscopic RVE, $\mathcal{V}_\diamond(\mathbf{x})$. In the following, the homogenisation of the constitutive law of polycrystalline materials defined in Section **??** will be explained.

- **Strain averaging**: the volume average of the microscopic strain $\boldsymbol{\varepsilon}^f$ over an RVE, $\mathcal{V}_\diamond(\mathbf{x})$, is defined as the macroscopic strain $\boldsymbol{\varepsilon}^c$ at the associated macroscopic point $\mathbf{x}$ [49] :

$$\boldsymbol{\varepsilon}^c(\mathbf{x},t) = \langle \boldsymbol{\varepsilon}^f \rangle \ = \ \frac{1}{|\mathcal{V}_\diamond(\mathbf{x})|} \int_{\partial V} \frac{1}{2}(\mathbf{u}^f \otimes \mathbf{n}_\Gamma + (\mathbf{u}^f \otimes \mathbf{n}_\Gamma)^T)\, \mathrm{d}\Gamma, \tag{44}$$

  where $|\mathcal{V}_\diamond(\mathbf{x})|$ is the surface area of the two-dimensional RVE, $\mathbf{n}_\Gamma$ denotes the unit outward vector normal to the RVE boundary, ∂V, and the tensor product operator is denoted by $\otimes$.

- **Stress averaging**: the coarse scale stress $\boldsymbol{\sigma}^c$ can be defined as the volume average of the microscopic

stress $\boldsymbol{\sigma}^f$ over the RVE, $\mathcal{V}_\diamond(\mathbf{x})$

$$\boldsymbol{\sigma}^c(\mathbf{x},t) \;=\; \langle \boldsymbol{\sigma}^f \rangle \;=\; \frac{1}{|\mathcal{V}_\diamond(\mathbf{x})|}\int_{\partial V} \mathbf{t}^f \otimes \mathbf{x}^f \, \mathrm{d}\Gamma, \tag{45}$$

In Eq. (45), the average stress is defined in terms of the boundary tractions $\mathbf{t}^f$, and the local coordinates at the RVE scale, $\mathbf{x}^f$ [49].

- **Strain energy averaging (Hill-Mandel condition)**: the Hill-Mandel condition which expresses the energy consistency of the micro-macro scale transition states that the volume average rate of work of any admissible microscale stress and strain rates over an RVE equals the rate of work of the average stress over the RVE [28]:

$$\boldsymbol{\sigma}^c : \dot{\boldsymbol{\varepsilon}}^c \;=\; \langle \boldsymbol{\sigma}^f : \dot{\boldsymbol{\varepsilon}}^f + \mathbf{t}^f \cdot [\![\dot{\mathbf{u}}^f]\!] \rangle \;=\; \langle \boldsymbol{\sigma}^f \rangle : \langle \dot{\boldsymbol{\varepsilon}}^f \rangle. \tag{46}$$

where $\mathbf{t}^f \cdot [\![\dot{\mathbf{u}}^f]\!]$ is the rate of work of traction $\mathbf{t}^f$ on the cohesive interfaces. This equality ensures that the homogenized stiffness tensor defined through the average of stress work equals to the same defined through the relations of the average of stress-strain. This energy consistency is automatically ensured if the stress and strain averaging are correctly made.

In order to track down the coarse scale constitutive law (69), a boundary value problem is defined over the RVE by imposing the prescribed fully bounded displacement boundary condition that is compatible with the strain averaging theorem (44). We recall that the constitutive laws of the fine scale constituents are explicitly defined. Hence, locally in the coarse domain, we assume the existence of an equilibrated micro pair $(\mathbf{u}^f, \boldsymbol{\sigma}^f)$defined over $\mathcal{V}_\diamond(\mathbf{x})$ such that the governing equations introduced in Eqs. (1), (2) and (3) are satisfied. The weak form of the governing equations is given by:

$$\forall \delta\mathbf{u}^f \in \mathcal{U}^{f,0}, \quad \int_{V/\Gamma^f} \boldsymbol{\sigma}^f : \boldsymbol{\varepsilon}(\delta\mathbf{u}^f)\, \mathrm{d}\Omega + \int_{\Gamma^f} \mathbf{T}^f \cdot [\![\delta\mathbf{u}^f]\!]\, \mathrm{d}\Gamma = 0, \tag{47}$$

where V is the RVE domain, and Γ^f is all the cohesive interfaces in the RVE.

$$\mathcal{U}^f = \left\{ \mathbf{u} | \mathbf{u} \in H^1(\Omega^f \setminus \Gamma^f), \mathbf{u}_{|_{\partial\Omega_D}} = \mathbf{u}_D^f \right\}, \tag{48}$$

$$\mathcal{U}^{f,0} = \left\{ \delta\mathbf{u} | \delta\mathbf{u} \in H^1(\Omega^f \setminus \Gamma^f), \delta\mathbf{u}_{|_{\partial\Omega_D}} = \mathbf{0} \right\}, \tag{49}$$

$$\tag{50}$$

This means that the RVE is in static equilibrium without prescribed tractions on the boundary and without volume body force. $\mathcal{U}^f$ and $\mathcal{U}^{f,0}$ are the collections of trial solutions, $\mathbf{u}^f$, and test functions, $\delta\mathbf{u}^f$, respectively. The constitutive equations for the microstructure have been discussed in Section **??**.

Downscaling kinematic condition: the following Dirichlet boundary condition which satisfies the strain averaging theorem (44) is imposed on the RVE problem:

$$\mathbf{u}_D^f(\mathbf{x}^f, t) = \boldsymbol{\varepsilon}^c(\mathbf{x}, t)\, \mathbf{x}^f \quad \text{on } \partial\Omega \tag{51}$$

where the macroscopic strain tensor $\boldsymbol{\varepsilon}^c(\mathbf{x}, t)$ at macroscopic point x and time t corresponding to the RVE $\mathcal{V}_\diamond(\mathbf{x})$. The center of RVEs is considered as the origin of the fine scale coordinate system $\mathbf{x}^f$. This particular choice for the boundary conditions of the RVE problem enforces that the fluctuation of the displacement field is null over the boundary. The choice of the fluctuation of the displacement field has an influence on the accuracy of homogenisation which is beyond the scope of this work [26].

Solving the RVE boundary value problem: The finite element method is used to solve the RVE problem defined by Eq. (47), and the Lagrange multiplier technique is adopted to impose the displacement boundary conditions (51):

$$\mathbf{R}_f^{\diamond}(\mathbf{U}^f, \boldsymbol{\lambda}) = \mathbf{f}_{\text{int}}^{\diamond} - \mathbf{f}_{\text{ext}}^{\diamond} - \mathbf{A}_{bf}^T \boldsymbol{\lambda} = \mathbf{0}, \tag{52}$$

$$\mathbf{R}_u^{\diamond}(\mathbf{U}^f) = \mathbf{A}_{bf}\mathbf{U}^f - \mathbf{u}_D^f = \mathbf{0}, \tag{53}$$

where $\mathbf{R}_f^{\diamond}$ and $\mathbf{R}_u^{\diamond}$ are the residual forces and residual displacements of the RVE, respectively. $\mathbf{U}^f$ is the nodal displacement at the fine scale, $\boldsymbol{\lambda}$ are the Lagrange multipliers, and $\mathbf{A}_{bf}$ is a boolean matrix that extracts the DOFs of the boundary from the total DOFs of the RVE. For our RVE boundary value problem, the equations for calculation of the external force $\mathbf{f}_{\text{ext}}^{\diamond} = \mathbf{0}$ and the internal force vector $\mathbf{f}_{\text{int}}^{\diamond}$ is given by Eq. (36). Note that Eq. (36) is given for a general microscale problem which can be adopted for the RVE boundary value problem.

The constitutive relationships for the microstructure are given by Eqs.(5) and (7). The non-linear system of equations (52) and (53) are linearised and set to zero in order to employ the Newton-Raphson iterative solver:

$$\begin{aligned}\bar{\mathbf{R}}_f^{\diamond}(\mathbf{U}^f + \Delta\mathbf{U}^f, \boldsymbol{\lambda} + \Delta\boldsymbol{\lambda}) =& \mathbf{R}_f^{\diamond}(\mathbf{U}^f, \boldsymbol{\lambda}) + \\ & \frac{\partial \mathbf{R}_f^{\diamond}(\mathbf{U}^f, \boldsymbol{\lambda})}{\partial \mathbf{U}^f}\Delta\mathbf{U}^f + \frac{\partial \mathbf{R}_f^{\diamond}(\mathbf{U}^f, \boldsymbol{\lambda})}{\partial \boldsymbol{\lambda}}\Delta\boldsymbol{\lambda} = \mathbf{0}\end{aligned} \tag{54}$$

$$\bar{\mathbf{R}}_u^{\diamond}(\mathbf{U}^f + \Delta\mathbf{U}^f) = \mathbf{R}_u^{\diamond}(\mathbf{U}^f) + \frac{\partial \mathbf{R}_u^{\diamond}(\mathbf{U}^f)}{\partial \mathbf{U}^f}\Delta\mathbf{U}^f = \mathbf{0}. \tag{55}$$

The resultant system of equations can be written in matrix form:

$$\begin{pmatrix} \overset{\diamond}{\mathbf{K}}_T & p\mathbf{A}_{bf}^T \\ p\mathbf{A}_{bf} & \mathbf{0} \end{pmatrix} \begin{pmatrix} \Delta\mathbf{U}^f \\ \Delta\bar{\boldsymbol{\lambda}} \end{pmatrix} = - \begin{pmatrix} \mathbf{R}_f^{\diamond}(\mathbf{U}^f, \boldsymbol{\lambda}) \\ \mathbf{R}_u^{\diamond}(\mathbf{U}^f) \end{pmatrix}, \tag{56}$$

where the entries of right hand side vector are given by Eqs. (52) and (53), and the tangent stiffness of the RVE, $\overset{\diamond}{\mathbf{K}}_T$, is given by Eq. (42). The Lagrange multipliers $\boldsymbol{\lambda}$ are replaced by $p\bar{\boldsymbol{\lambda}}$ to improve the condition number of the global stiffness matrix, as $p = \max(|\overset{\diamond}{\mathbf{K}}_{ii}|)$ is a scalar related to the maximum diagonal entry of the initial stiffness matrix of RVE. It is calculated once at the beginning of simulation [62].

Up-scaling kinetic condition: After solving the RVE problem, the Lagrange multipliers $\boldsymbol{\lambda}$ represent the traction on the boundary of the RVE and can be used in Eq. (45) to upscale the macroscopic stress:

$$\begin{aligned}\boldsymbol{\sigma}^c(\mathbf{x}, t) &= \frac{1}{|\mathcal{V}_{\diamond}(\mathbf{x})|}\int_{\partial V} \mathbf{t}^f \otimes \mathbf{x}^f \, \mathrm{d}\Gamma \\ &= \frac{1}{|\mathcal{V}_{\diamond}(\mathbf{x})|}\sum_{e=1}^{n_b}\left(\int_{\partial V_e \cap \partial V} \mathbf{t}_e^f \, [N_1 \;\; N_2]_e \, \mathrm{d}\Gamma \begin{bmatrix} x_1^f & y_1^f \\ x_2^f & y_2^f \end{bmatrix}_e\right) \\ &= \frac{1}{|\mathcal{V}_{\diamond}(\mathbf{x})|}\sum_{e=1}^{n_b}\left(\int_{\partial V_e \cap \partial V} \begin{bmatrix} t_x^f N_1 & t_x^f N_2 \\ t_y^f N_1 & t_y^f N_2 \end{bmatrix}_e \mathrm{d}\Gamma \begin{bmatrix} x_1^f & y_1^f \\ x_2^f & y_2^f \end{bmatrix}_e\right) \\ &= \frac{1}{|\mathcal{V}_{\diamond}(\mathbf{x})|}\sum_{e=1}^{n_b}\begin{bmatrix} \lambda_{x_1} & \lambda_{x_2} \\ \lambda_{y_1} & \lambda_{y_2} \end{bmatrix}_e \begin{bmatrix} x_1^f & y_1^f \\ x_2^f & y_2^f \end{bmatrix}_e,\end{aligned} \tag{57}$$

where n_b is the number of the elements that have an edge on the boundary of RVE. N_1 and N_2 are the shape functions of the first and second nodes on that edge of element e that is common with the boundary of RVE,

$\partial V_e \cap \partial V \neq \emptyset$. The position of the quadrature points on the element edge are given by interpolation of nodal positions using the finite element shape functions:

$$\mathbf{x}_e^f = [N_1 \;\; N_2]_e \begin{bmatrix} x_1^f & y_1^f \\ x_2^f & y_2^f \end{bmatrix}_e, \tag{58}$$

The matrix of the node positions $[x_i,\ y_i]_e$ ($i = \{1, 2\}$) is constant, and can be out of integral. In the last line of Eq. (57), $\int \mathbf{t}^f N_i \, \mathrm{d}\Gamma$ gives the boundary integral of external traction $\mathbf{t}^f$ over external boundary of element e that in the finite element method, equals the nodal force $[\lambda_{x_i}, \lambda_{y_i}]_e$. Therefore, the macroscopic stress in Voigt form can be computed by:

$$\boldsymbol{\sigma}^c(\mathbf{x}, t) = \frac{1}{|\mathcal{V}_\diamond(\mathbf{x})|} \mathbf{D}^T \boldsymbol{\lambda}, \tag{59}$$

where

$$\mathbf{D}^T = \begin{bmatrix} x_1^f & 0 & x_2^f & 0 & \cdots & x_{n_b}^f & 0 \\ 0 & y_1^f & 0 & y_2^f & \cdots & 0 & y_{n_b}^f \\ 0.5y_1^f & 0.5x_1^f & 0.5y_2^f & 0.5x_2^f & \cdots & 0.5y_{n_b}^f & 0.5x_{n_b}^f \end{bmatrix}. \tag{60}$$

The macroscopic tangent stiffness $\mathbf{C}_T$ is determined by finding the relationship between $\Delta\boldsymbol{\sigma}^c = \langle \Delta\boldsymbol{\sigma}^f \rangle$ and $\Delta\boldsymbol{\varepsilon}^c = \langle \Delta\boldsymbol{\varepsilon}^f \rangle$ through the finite element solution of the RVE problem. Recall Eqs. (51) and (59), the variation of macroscopic stress and strain can be given by:

$$\Delta\mathbf{u}_D^f = \mathbf{D}\Delta\boldsymbol{\varepsilon}^c, \tag{61}$$

$$\Delta\boldsymbol{\sigma}^c = \frac{1}{|\mathcal{V}_\diamond(\mathbf{x})|} \mathbf{D}^T \Delta\boldsymbol{\lambda}. \tag{62}$$

On the other hand, the relation between $\Delta\mathbf{u}_D^f$ and $\Delta\boldsymbol{\lambda}$ can be defined through the Schur complement of the tangent stiffness matrix with respect to the internal nodes of the RVE $\Delta\boldsymbol{\lambda} = \overset{\diamond}{\mathbf{K}}_S \ \Delta\mathbf{u}_D^f$. Thus the macroscopic stress-strain relationship can be defined by:

$$\Delta\boldsymbol{\sigma}^c = \frac{1}{|\mathcal{V}_\diamond(\mathbf{x})|} \mathbf{D}^T \ \overset{\diamond}{\mathbf{K}}_S \ \mathbf{D} \ \Delta\boldsymbol{\varepsilon}^c, \tag{63}$$

where $\overset{\diamond}{\mathbf{K}}_S = \overset{\diamond}{\mathbf{K}}_{bb} - \overset{\diamond}{\mathbf{K}}_{bi} \overset{\diamond}{\mathbf{K}}_{ii}^{-1} \overset{\diamond}{\mathbf{K}}_{ib}$. Consequently, the macroscopic tangent stiffness $\mathbf{C}_T$ is

$$\mathbf{C}_T = \frac{1}{|\mathcal{V}_\diamond(\mathbf{x})|} \mathbf{D}^T \ \overset{\diamond}{\mathbf{K}}_S \ \mathbf{D}. \tag{64}$$

An algorithm for the FE^2 method applied to out problem of fracture in polycrystalline materials is shown in Figure 8.

3.1.2. Limitations

In the previous section, a computational homogenisation multiscale method was presented. Despite a number of attractive characteristics, there are a few significant limitations to the this computational homogenisation framework which are described, for instance [35, 26, 22]. The main limitations of homogenisation are:

- Bridging scales by homogenisation are only valid if scales are separable. The main shortcomings of classical homogenisation schemes come from the fundamental implicit assumption that the RVE size must be negligible in comparison with the macro structural characteristic length (determined by the size of the macroscopic specimen or the wave length of the macroscopic load) [28]. While softening

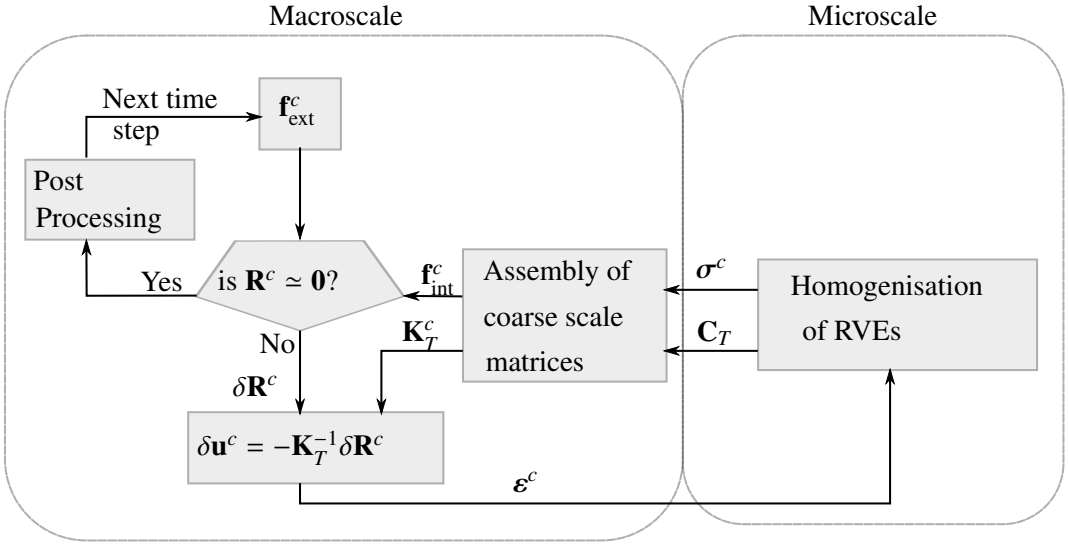

Figure 8: FE^2 scheme.

happens, the homogenisation method is strongly sensitive to the variation of both macroscopic mesh size and RVE size.

- This is a computationally expensive method but it is much cheaper than solving engineering problems fully at the microscale. However, novel methods aim at reducing this computational effort. For instance nonuniform transformation field analysis, [47]; Model order reduction [32]) and more heuristic ones where RVE is deactivated or RVEs are regrouped.

According to the first shortcoming, bridging scales by homogenisation are only valid if scales are separable. In the critical regions where the scale separation assumption is not fulfilled, the FE^2 method is bypassed and a concurrent multiscale method is adopted. In the concurrent multiscale method the scale separation assumption does not need to be fulfilled, since the microscopic model is solved directly.
In the next section, a concurrent multiscale method based on domain decomposition is detailed, in order to solve the microscopic problem in critical regions simultaneously with the macroscopic problem.

3.2. Macroscopic problem

When the characteristic length of the problem at the loading scale, L, is considerably larger than the characteristic length of the microstructure, l (see Fig. 1) computational homogenisation can be employed to search for an effective displacement field $\mathbf{u}^c \in \mathcal{U}^c$ defined over Ω which

$$\forall \delta\mathbf{u}^c \in \mathcal{U}^{c,0}, \quad \delta\Pi = \int_\Omega \boldsymbol{\sigma}^c_{|_t} : \boldsymbol{\varepsilon}(\delta\mathbf{u}^c)\, \mathrm{d}\Omega - \int_{\partial\Omega_N} \mathbf{F}_{|_t} \cdot \delta\mathbf{u}^c\, \mathrm{d}\Gamma = 0. \tag{65}$$

$\mathcal{U}^c$ and $\mathcal{U}^{c,0}$ are collections of trial functions, $\mathbf{u}$, and test functions, $\delta\mathbf{u}$, respectively, which can be defined by

$$\mathcal{U}^c = \left\{\mathbf{u} | \mathbf{u} \in H^1(\Omega), \mathbf{u}_{|\partial\Omega_D} = \mathbf{u}_D\right\}, \tag{66}$$

$$\mathcal{U}^{c,0} = \left\{\mathbf{u} | \mathbf{u} \in H^1(\Omega), \delta\mathbf{u}_{|\partial\Omega_N} = \mathbf{0}\right\}, \tag{67}$$

where H^1 is the Sobolev space of degree one. This is because the solution at the coarse scale is smoothed through homogenisation, and microscopic cracks at the crystalline scale is represented by reduction in the

macroscopic stiffness. The Dirichlet boundary condition at all times is given by

$$\mathbf{u}^c_{|\mathbf{x},t} = \mathbf{u}_{D|\mathbf{x},t} \quad \text{on } \partial\Gamma_D. \tag{68}$$

The Homogenised constitutive law at the coarse scale relates the coarse stress to the history of the coarse strain, locally at every point of the domain:

$$\boldsymbol{\sigma}^c_{|\mathbf{x},t} = \sigma^c\left(\left(\boldsymbol{\varepsilon}(\mathbf{u}^c_{|\mathbf{x},\mathcal{T}})\right)_{\mathcal{T}\leq t}\right) \quad \text{in } \Omega, \tag{69}$$

where $\boldsymbol{\sigma}^c$ and $\boldsymbol{\varepsilon}^c$ are the coarse scale stress and strain respectively. In the general framework of homogenisation, the coarse scale constitutive law (69) is not known *a priori*. It is assumed however that, at lower scales, the constitutive law of the microstructural heterogeneities is known, or is at least identifiable. The

coarse scale problem Eq. (65) is spatially discretised by triangular linear finite elements. One integration point suffices for each element. Finally, the finite element discretisation of Eq. (65) can be written as:

$$\delta\Pi = \delta\mathbf{U}^{cT}\left(\sum_e \mathbf{M}_e \int_{\Omega^c_e\ \Gamma^c} \mathbf{B}^{cT}_e \boldsymbol{\sigma}^c_e \,\mathrm{d}\Omega - \sum_e \mathbf{M}_e \int_{\partial\Omega_N} \mathbf{N}_e{}^T \mathbf{F}\,\mathrm{d}\Gamma\right) = 0. \tag{70}$$

where $\mathbf{N}_e$ and $\mathbf{B}^c_e$ are shape function matrix and derivaties of the shape functions for the triangular linear coarse elements which are given by (28) and (29) respectively. $\boldsymbol{\sigma}^c_e$ is the vector form of stress, and $\mathbf{M}_e$ is the boolean matrix that maps the coarse element vector to the corresponding entries of the global vector. Since the variational work is zero for any admissible variation of displacement vector $\delta\mathbf{U}^c$, it is concluded that the residual force vector must be null:

$$\mathbf{R}^c\left(\mathbf{U}^c\right) = \mathbf{f}_{\text{int}}\left(\mathbf{U}^c\right) - \mathbf{f}_{\text{ext}} = \mathbf{0}, \tag{71}$$

where

$$\mathbf{f}_{\text{int}}\left(\mathbf{U}^c\right) = \sum_e \mathbf{M}_e \int_{\Omega^c_e} \mathbf{B}^{cT}_e \boldsymbol{\sigma}^c_e \,\mathrm{d}\Omega \tag{72}$$

$$\mathbf{f}_{\text{ext}} = \sum_e \mathbf{M}_e \int_{\partial\Omega_N} \mathbf{N}_e{}^T \mathbf{F}\,\mathrm{d}\Gamma. \tag{73}$$

Because of material non-linearity, Eq. (71) cannot be solved directly for $\mathbf{U}^c$. The Newton-Raphson procedure is employed to find the solution iteratively. The linearisation of the coarse scale residual $\mathbf{R}^c$ with respect to the displacement $\mathbf{U}^c$ is given by:

$$\bar{\mathbf{R}}^c\left(\mathbf{U}^c + \Delta\mathbf{U}^c\right) = \mathbf{R}^c\left(\mathbf{U}^c\right) + \frac{\partial \mathbf{R}^c}{\partial \mathbf{U}^c}\Delta\mathbf{U}^c = 0, \tag{74}$$

finally the linearised equilibrium equation for the coarse scale problem can be written as

$$\mathbf{K}^c_T \Delta\mathbf{U}^c = -\left(\mathbf{f}_{\text{int}}\left(\mathbf{U}^c\right) - \mathbf{f}_{\text{ext}}\right) \tag{75}$$

where after each iteration, the displacement vector $\mathbf{U}^c$ is updated, and consequently the internal force vector $\mathbf{f}_{\text{int}}\left(\mathbf{U}^c\right)$ and the tangent stiffness matrix $\mathbf{K}^c_T$ is updated by solving the underlying RVE problem. The tangent stiffness matrix is

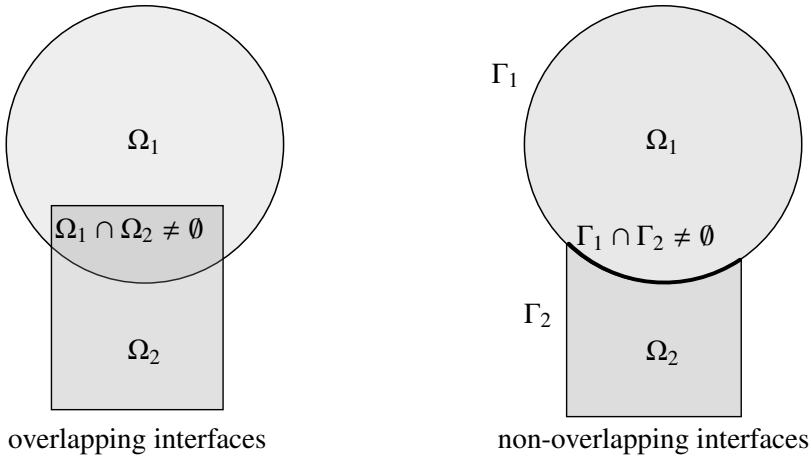

Figure 9: Overlapping and non-overlapping domain decomposition methods.

$$\mathbf{K}_T^c = \frac{\partial \mathbf{f}_{\text{int}}}{\partial \mathbf{U}^c} = \sum_e \mathbf{M}_e \left(\int_{\Omega_e^c} \mathbf{B}_e^{cT} \frac{\partial \boldsymbol{\sigma}_e^c}{\partial \boldsymbol{\varepsilon}_e^c} \frac{\partial \boldsymbol{\varepsilon}_e^c}{\partial \mathbf{U}_e^c} \, \mathrm{d}\Omega \right) \mathbf{M}_e^T$$
$$= \sum_e \mathbf{M}_e \left(\int_{\Omega_e^c} \mathbf{B}_e^{cT} \mathbf{C}_{T_e} \mathbf{B}_e^c \, \mathrm{d}\Omega \right) \mathbf{M}_e^T \tag{76}$$

where $\mathbf{C}_{T_e}$ is the macroscopic tangent stiffness that is computed through the homogenisation of the constitutive law given Eq. (64). When the component of residual force $\mathbf{R}^c(\mathbf{U}^c)$ become "very small" (less than some convergence tolerance) the Newton-Raphson iterations are stopped, and a new time step is started by changing the external force $\mathbf{f}_{\text{ext}}$.

3.3. Concurrent Multiscale: Domain Decomposition Method

Domain decomposition methods (DDM) can be used for solving a large problem by partitioning it into smaller subdomains or for solving a problem with different physical models in its sub-domains [40, 18, 43, 36].

Figure 9 shows the two main classes of Domain decomposition methods: overlapping [16, 27] and non-overlapping [38, 41] interface methods. DDM can also be categorised into direct and iterative.

For our problem, a non-overlapping DDM is adopted to solve directly the microscopic problem at a critical region concurrently along with the coarse scale problem at the region that scales are separable (see Fig. 10). The domain Ω is partitioned into a coarse scale sub-domain Ω^c and a fine scale sub-domain Ω^f such that $\Omega^c \cup \Omega^f = \Omega$ and $\Omega^c \cap \Omega^f = \emptyset$. The FE^2 method is used to solve the microscopic problem on average over Ω^c. The finite element method is deployed to directly model the microscopic problem at the fine scale Ω^f. Figure 10 depicts schematically the hybrid multiscale scheme for modelling of fracture in polycrystalline materials. It is assumed that there is an equation that bridges the fine scale to the coarse scale solutions:

$$\mathbf{R}^\Gamma \left(\mathbf{u}^c, \mathbf{u}^f \right) = \mathbf{0}, \quad \text{on } \Gamma^{fc}. \tag{77}$$

where $\mathbf{u}^f$ and $\mathbf{u}^c$ are the displacement field at the Ω^f and Ω^c, respectively.

The Lagrange multiplier technique is used to satisfy the constraint equation 77. At a stationary point, the variation of the Lagrangian function Λ with respect to the displacement of the coarse scale $\delta\mathbf{u}^c$, the displacement of the fine scale $\delta\mathbf{u}^f$, and the Lagrange multipliers $\delta\boldsymbol{\lambda}$ vanish and provide the equilibrium equation for the domain Ω:

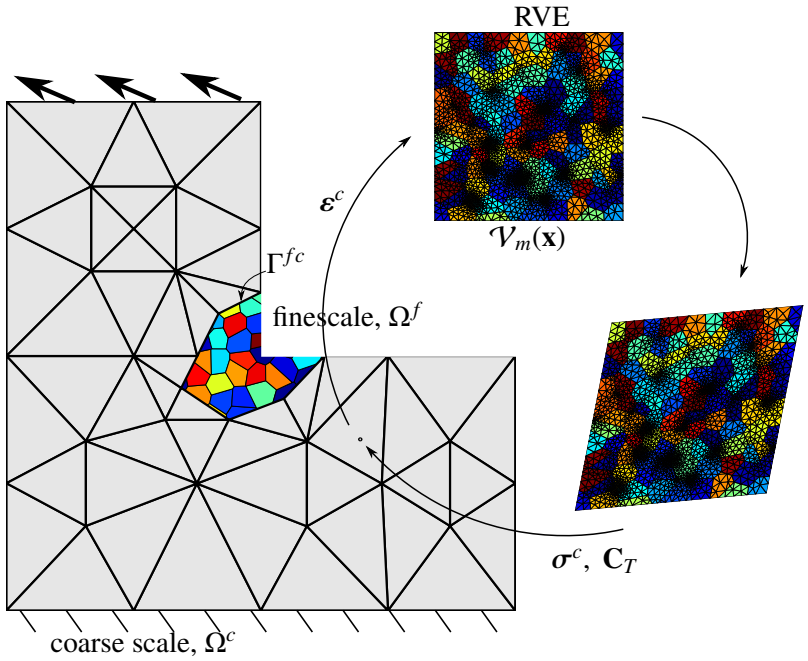

Figure 10: A hybrid multiscale method includes non-overlapping domain decomposition method and FE^2. See also Fig.12

$$\frac{\partial \Lambda}{\partial \mathbf{u}^c} \cdot \delta \mathbf{u}^c = \delta \Pi^c(\mathbf{u}^c, \delta \mathbf{u}^c) + \boldsymbol{\lambda} \cdot \frac{\partial \mathbf{R}^\Gamma(\mathbf{u}^c, \mathbf{u}^f)}{\partial \mathbf{u}^c} \delta \mathbf{u}^c = \mathbf{0}, \tag{78}$$

$$\frac{\partial \Lambda}{\partial \mathbf{u}^f} \cdot \delta \mathbf{u}^f = \delta \Pi^f(\mathbf{u}^f, \delta \mathbf{u}^f) + \boldsymbol{\lambda} \cdot \frac{\partial \mathbf{R}^\Gamma(\mathbf{u}^c, \mathbf{u}^f)}{\partial \mathbf{u}^f} \delta \mathbf{u}^f = \mathbf{0}, \tag{79}$$

$$\frac{\partial \Lambda}{\partial \boldsymbol{\lambda}} \cdot \delta \boldsymbol{\lambda} = \mathbf{R}^\Gamma \cdot \delta \boldsymbol{\lambda} = \mathbf{0}. \tag{80}$$

where the $\boldsymbol{\lambda}$ are Lagrange multipliers. It is noted that the arbitrary variation of displacement fields must be null on the Dirichlet boundary, $\delta \mathbf{u}(\mathbf{x}) = \mathbf{0} \quad \forall \mathbf{x} \in \partial\Omega_D$. The variation of the virtual works in the coarse scale $\delta\Pi^c$ and in the fine scale $\delta\Pi^f$ after discretization by finite elements are given by Eqs. (70) and (22) respectively. In the following, the choice of constraint equation (77) is discussed.

3.4. Coupling Fine-Coarse meshes

Coupling techniques can be divided into two main categories: strong and weak couplings. In strong coupling the fluctuation of microscopic displacement on the interface vanishes, while in weak coupling techniques fluctuations exist but its weighted average is zero on the coarse-fine interface. Figure 11 shows difference between weak and strong coupling schematically.

For a microstructure with discrete cracks, employing a weak coupling technique increases the condition number of the global stiffness matrix, and consequently the Newton-Raphson solver requires more iteration to converge [29, 54]. In other words, weak coupling techniques is more expensive in terms of computational cost. In this work, the linear multipoint constraint (LMPC) method [1, 19] is adopted to impose a strong coupling on the displacement at the interface between the fine and the coarse meshes. This coupling technique is based on Lagrange multipliers that strongly glue the fine solution to the coarse solution along the common interface. The coarse scale is discretized by linear triangular elements, and as discussed in Section **??**, the fine scale has been discretized by linear triangular elements, and four-node cohesive elements. The strong coupling between the fine scale nodal displacement and the coarse scale displacement at the interface Γ^{fc} is obtained by enforcing the micro nodes that belong to a macro edge to follow the edge deformation.

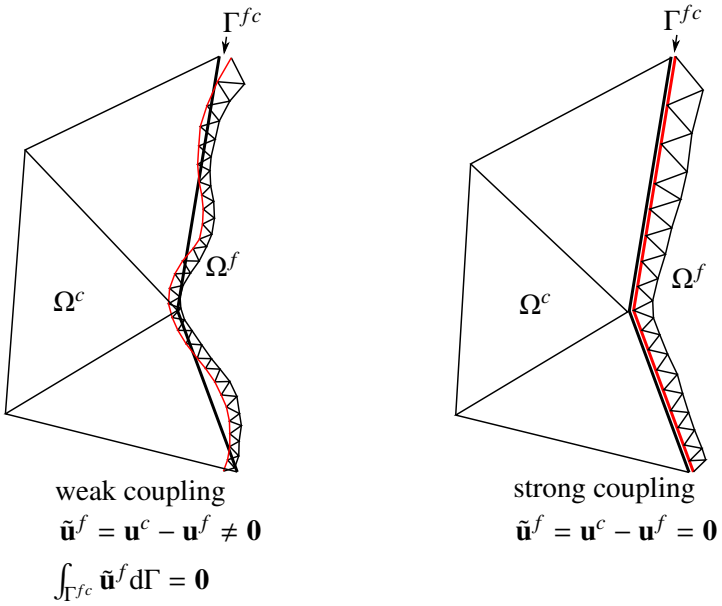

Figure 11: Strong coupling vs. weak coupling in non-overlapping DDM in deformed configuration.

For example, displacement of a fine mesh node i is enforced to follow the displacement of the edge of an adjacent coarse element e by using the coarse element shape functions $\bar{\mathbf{N}}_e$ on the interface

$$\mathbf{R}_i^{\Gamma}\left(\mathbf{U}_e^c, \mathbf{U}_i^f\right) = \mathbf{U}_i^f - \bar{\mathbf{N}}_e(\zeta_i)\mathbf{U}_e^c = \mathbf{0}, \quad \text{on } \Gamma_e^{fc}. \tag{81}$$

where ζ is the local coordinate system of the coarse element e at the interface, and $\mathbf{u}_e^c$ is the nodal displacement vector of the element (e) on the interface Γ^{fc}. The shape function $\bar{\mathbf{N}}_e$ is given by

$$\bar{\mathbf{N}}_e(\zeta) = \begin{bmatrix} 1 - \frac{\zeta}{l_e} & 0 & \frac{\zeta}{l_e} & 0 \\ 0 & 1 - \frac{\zeta}{l_e} & 0 & \frac{\zeta}{l_e} \end{bmatrix} \tag{82}$$

where l_e is the length of edge of element (e) on the interface Γ^{fc}. Figure 12 displays details of the LMPC method.

Equation (81) provides the constraint equations for the particular node i. The global constraint equations for all the nodes on the interface Γ^{fc} is given by:

$$\mathbf{R}^{\Gamma}\left(\mathbf{U}^c, \mathbf{U}^f\right) = \mathbf{A}^f\mathbf{U}^f - \mathbf{A}^c\mathbf{U}^c = \mathbf{0}, \tag{83}$$

The boolean matrix $\mathbf{A}^f$ is defined to extract all nodal displacements of the fine mesh that corresponds to the interface Γ^{fc}, and $\mathbf{A}^c$ is a matrix combining the values of shape functions of the coarse nodes on the interface Γ^{fc}. Note that the coarse mesh is expected to vary due to adaptivity during the multiscale analysis. For this reason, the structure of the matrix $\mathbf{A}^c$ needs to be recomputed as soon as the coarse mesh is refined.

3.5. Solving the coupled problem

In this coupling technique microscopic cracks with one end on the interface Γ^{fc} cannot open due to the strong coupling of displacements imposed by coarse scale continuum displacement (see node i in Fig. 12), as macroscopic displacements are continuous along the coupling region. Even though we are not going to model plasticity in the grains, it is worth mentioning that the strong coupling of displacements can generate an artificial plasticity in those grains that are next to the coarse nodes on the interface Γ^{fc}. This is due to the jump of the macroscopic strain along the edge of the coarse elements and also at the coarse nodes.

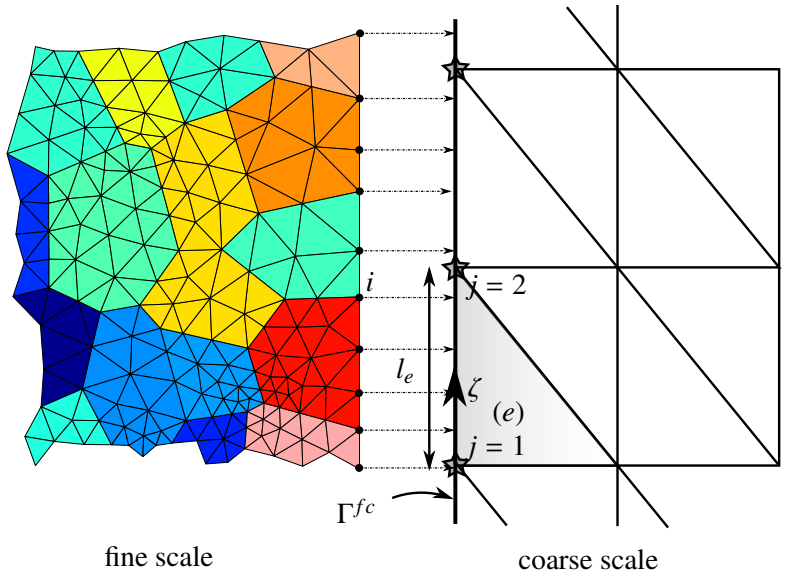

Figure 12: Strong coupling between the fine mesh and the coarse mesh using the linear multipoint constraint (LMPC) method.

By substituting the discretized form of Eqs. (70), (22) and (83) into the stationarity equations of Lagrangian functions (78), (79) and (80) a set of nonlinear equations for the domain Ω is obtained:

$$\begin{cases} \mathbf{R}^c\left(\mathbf{U}^c, \boldsymbol{\lambda}\right) = \mathbf{f}^c_{\text{int}}\left(\mathbf{U}^c\right) - \mathbf{f}^c_{\text{ext}} - \mathbf{A}^{cT}\boldsymbol{\lambda} = \mathbf{0}, \\ \mathbf{R}^f\left(\mathbf{U}^c, \boldsymbol{\lambda}\right) = \mathbf{f}^f_{\text{int}}\left(\mathbf{U}^f\right) - \mathbf{f}^f_{\text{ext}} + \mathbf{A}^{fT}\boldsymbol{\lambda} = \mathbf{0}, \\ \mathbf{R}^\Gamma\left(\mathbf{U}^c, \mathbf{U}^f\right) = \mathbf{A}^f\mathbf{U}^f - \mathbf{A}^c\mathbf{U}^c = \mathbf{0}. \end{cases} \tag{84}$$

Equation (84) is a nonlinear equation that needs to be linearised before solving by iterative solvers. The linearisation of the coarse mesh residual $\mathbf{R}^c$ with respect to its variables is given by:

$$\begin{aligned} \bar{\mathbf{R}}^c\left(\mathbf{U}^c + \Delta\mathbf{U}^c, \boldsymbol{\lambda} + \Delta\boldsymbol{\lambda}\right) = \mathbf{R}^c\left(\mathbf{U}^c, \boldsymbol{\lambda}\right) + \frac{\partial \mathbf{R}^c}{\partial \mathbf{U}^c}\Delta\mathbf{U}^c + \frac{\partial \mathbf{R}^c}{\partial \boldsymbol{\lambda}}\Delta\boldsymbol{\lambda} = \\ \mathbf{f}^c_{\text{int}}\left(\mathbf{U}^c\right) - \mathbf{f}^c_{\text{ext}} - \mathbf{A}^{cT}\boldsymbol{\lambda} + \mathbf{K}^c_T\Delta\mathbf{U}^c - \mathbf{A}^{cT}\Delta\boldsymbol{\lambda}. \end{aligned} \tag{85}$$

where $\mathbf{K}^c_T$ is the tangent stiffness of the coarse scale problem that was given in Eq. (76). The linearisation of the fine mesh residual $\mathbf{R}^f$ and interface residual $\mathbf{R}^\Gamma$ can be done in the same way. Finally a system of linear equations is obtained:

$$\begin{bmatrix} \mathbf{K}^c_T & \mathbf{0} & -p\mathbf{A}^{cT} \\ \mathbf{0} & \mathbf{K}^f_T & p\mathbf{A}^{fT} \\ -p\mathbf{A}^c & p\mathbf{A}^f & \mathbf{0} \end{bmatrix} \begin{Bmatrix} \Delta\mathbf{U}^c \\ \Delta\mathbf{U}^f \\ \Delta\bar{\boldsymbol{\lambda}} \end{Bmatrix} = -\begin{Bmatrix} \mathbf{R}^c \\ \mathbf{R}^f \\ \mathbf{R}^\Gamma \end{Bmatrix}. \tag{86}$$

Lagrange multipliers, $\boldsymbol{\lambda}$ are replaced by $p\bar{\boldsymbol{\lambda}}$ to avoid uncontrolled increase of the condition number of the system of equations, and $p = \max(|\mathbf{K}^c_{ii}|)$ is a scalar related to the maximum diagonal entry of the initial stiffness matrix of coarse problem and calculated once at the beginning of the simulation [62]. In Eq. (86) the external forces $\mathbf{f}^c_{\text{ext}}$ and $\mathbf{f}^f_{\text{ext}}$ are updated at each increment of the time step while the tangent stiffness matrices $\mathbf{K}^c_T$ and $\mathbf{K}^f_T$, and internal forces $\mathbf{f}^c_{\text{int}}$ and $\mathbf{f}^f_{\text{int}}$ are updated at each iteration due to the change in the

displacement and the Lagrange multipliers:

$$\mathbf{U}^c_{|i} = \mathbf{U}^c_{|i-1} + \Delta\mathbf{U}^c_{|i}, \tag{87}$$

$$\mathbf{U}^f_{|i} = \mathbf{U}^f_{|i-1} + \Delta\mathbf{U}^f_{|i}, \tag{88}$$

$$\boldsymbol{\lambda}_{|i} = \boldsymbol{\lambda}_{|i-1} + \Delta\boldsymbol{\lambda}_{|i}, \tag{89}$$

where subscripts $|i-1$ and $|i$ indicate the results for the previous iteration and the current iteration respectively. In the Newton-Raphson iterative schemes, after each increment, the initial residual forces are out of balance, $\mathbf{R}_{|i=0} \neq \mathbf{0}$. The resolution process is stopped when the relative euclidean norm of the residual at time step i, $\frac{\|\mathbf{R}_{|i}\|}{\|\mathbf{R}_{|i=0}\|}$ is smaller than an acceptable tolerance $\epsilon_{\mathbf{R}}$. In this problem, the residual force vector is composed of the out of balance vector $\left[\mathbf{R}^c,\ \mathbf{R}^f\right]^T$ and residual of the constraint equation $\mathbf{R}^\Gamma$ which may have values of different orders of magnitude. One must then normalize with predetermined quantities the various components of the residual or displacements vectors before assessing the convergence. In this DDM, the residual of the interface constraint is normalized using a scalar parameter, $\mathbf{R}^{\Gamma*} = p\mathbf{R}^\Gamma$ where $p = \max\left(|\mathbf{K}^c_{ii}|\right)$.

4. Solution Procedure

In order to model polycrystalline microstructures, the previous section presented a combination of two methods: a hierarchical multiscale method based on computational homogenisation (FE^2), and a concurrent multiscale method based on non-overlapping domain decomposition. The FE^2 method is unable to simulate materials in the region where localisation occurs (the corresponding RVE is in softening regime) or in a region where the homogenisation assumptions are not valid. In other words, when the balance equations of an RVE lose ellipticity, the principle of scale separation is not satisfied for that size of an RVE. Consequently, the averaging theorem on which FE^2 relies is not valid in the corresponding region. In contrast, concurrent multiscale methods can simulate localisation phenomena by splitting the domain into the damaging (or critical regions) and loading regions.

We propose a hybrid method, a combination of the FE^2 method and domain decomposition, which removes these shortcomings. The FE^2 technique is used in the regions of the structure that are in a loading regime, i.e not damaging beyond the material stability limit, where representative volume elements satisfy the principle of scale separation. In the critical regions where localisation occurs, a domain decomposition scheme is used to solve the problem exactly at the scale of the material heterogeneities. In order to control the precision of the simulations, error estimation for the up-scaling strategy is carried out at each step of the time integration algorithm. Based on this estimation, the coarse elements are refined hierarchically where needed. When the homogenisation error exceeds a critical value, the homogenisation step is bypassed, and the corresponding critical region is modelled directly at the microscale. First a zoom-in [41] process is performed in which the critical region fully resolved at the microscale using boundary conditions based on the history of displacement of the corresponding coarse elements. The fully resolved region is coupled to the coarse mesh and a relaxation process is performed to eliminate the out-of-balance internal forces due to the replacement of the critical coarse elements by the new finer mesh. Thereafter, the fully resolved region and homogenised region are solved concurrently in the domain decomposition framework (LMPC) which was explained in Section 3.4. In order to follow progressive failure, the fully resolved region is adaptively extended.

Inspired by [42] and [31], a local arc-length technique is developed for the multiscale domain decomposition problem which follows the load-displacement curve by imposing a constraint over the maximum increment for the jump of all cohesive interface within the fully resolved regions. This is detailed in the following section.

4.1. Error Estimation and Adaptive Mesh Refinement

Errors arisen from the finite element solution of an engineering problem can be categorised into three groups:

- modelling error: This error is related to the mathematical modelling of the problem, e.g. mathematical model for the constitutive relationship and boundary conditions. In FE^2 method, the error in homogenisation can be interpreted as the modelling error.

- discretisation error: This error arises from representing the continuous solution space of the mathematical model by the discretised solution of finite element method.

- solution error: This source of the error is due to the computational process of the finite element solution, e.g. numerical integration.

The finite element method provides an approximation for the exact solution, and the difference between these two solutions is called the discretisation error,e_d , which can usually be reduced by the refinement of elements. Several discretisation error estimators have been developed in the literature which can be classified as *a posteriori* and *a priori* [2, 9]. In this thesis, an *a posteriori* Zienkiewicz-Zhu recovery-based error estimator is adopted to control the coarse scale discretisation error by the local refinement of coarse elements.
In addition to the discretisation error, an FE^2 solution can be polluted by a homogenisation error, e_h, caused by the partial fulfilment of the scale separation assumption, the boundary conditions and the finite element discretisation of the RVE [37, 59]. In this work, errors emanating from the boundary condition and the finite element discretisation of the RVE are not considered. In first order homogenisation, it is assumed that the macroscopic strain is constant in the vicinity of the sampling point corresponding to each RVE. This assumption is violated in regions with highly localised deformation. In such regions, second order homogenisation can provide more accurate results in comparison to first order homogenisation since the gradient of strain field is not truncated in second order homogenisation. The modelling error indicator for first order homogenisation, proposed by [59], is adopted to measure the homogenisation error in the FE^2 method. Thereafter, a critical value can be defined for the first order homogenisation error, which controls the scale adaptation procedure.

4.2. Homogenisation error

In order to determine the loss of accuracy for first order homogenisation [59] and [64] developed two error indicators. The main concept of their error indicators is based on the difference between the strain energy from second order homogenisation and the strain energy from the first order homogenisation. [59] solved homogenisation of a hyperelastic unit cell with differing degrees of material heterogeneity, and different deformation and gradient of deformation at the macroscale. By comparing the results from first order and second order homogenisation, they have shown that the major quantity controlling the deviation from a first-order framework is $L_{\mathcal{V}}\|\nabla\nabla\mathbf{u}^c\|$ which they referred to as the strain-gradient sensitivity. $L_{\mathcal{V}}$ is the size of the RVE, and $\|\nabla\nabla\mathbf{u}^c\|$ is the L_2 norm of the second gradient of the displacement field that can be written in indicial notation as $\|\nabla\nabla\mathbf{u}^c\| = \sqrt{u^c_{i,jk}u^c_{i,jk}}$. Inspiring by [64] and [59], the strain-gradient sensitivity $e_h = L_{\mathcal{V}}\|\nabla\nabla\mathbf{u}^c\|$ is considered as the error of first order homogenisation e_h by assuming that the effect of microstructure heterogeneity on the homogenisation error is bounded.
Since the second displacement gradient varies proportionally to the inverse of the coarse scale element size $\|\nabla\nabla\mathbf{u}^c\| \propto \frac{1}{h}$ [59], coarse mesh refinement on the one hand decrease the discretisation error, and on the other hand, increases the homogenisation error. The variation of homogenisation error and discretisation error versus the coarse element size are depicted in Fig. 13. In [64], a critical size for the coarse element has been defined such that if the size of a coarse element is less than the critical size, then homogenisation is bypassed, since the homogenisation error is beyond the permissible value.
In this work, instead of choosing a critical element size, a critical value for the homogenisation error $e_h^{\text{crit}} = 0.01$ is directly considered as a flag for adaptation of scale such that if:

$$L_{\mathcal{V}}\|\nabla\nabla\mathbf{u}^c\|_e > e_h^{\text{crit}}, \tag{90}$$

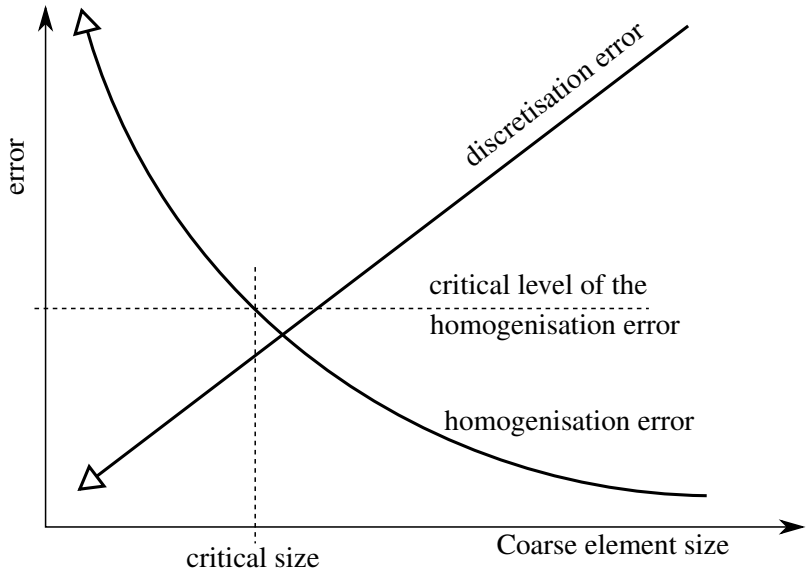

Figure 13: The variation of homogenisation error and discretisation error with respect to the coarse element size in FE^2 [64].

then the corresponding coarse element e must be replaced by a model of the background microscopic structure. Due to the coarse linear elements employed in this work, the second gradient of the macroscopic displacement is zero everywhere. Therefore the method proposed in [59] which relies on a non-zero second displacement gradient, cannot be used directly. To have a non-zero gradient of strain field at the coarse scale, we propose to adopt the averaging technique used in recovery-based error estimation [68] to obtain nodal values of the displacement gradient, and consequently, a constant stepwise second displacement gradient is obtained over the coarse elements. The displacement gradient tensor for each element $\nabla \mathbf{u}^c = \frac{\partial u_i}{\partial x_j}$ can be be obtained in vector form:

$$\forall e \in \Omega^c, \quad \nabla \mathbf{u}^c_e = \begin{Bmatrix} \frac{\partial u^c}{\partial x} \\ \frac{\partial v^c}{\partial y} \\ \frac{\partial u^c}{\partial y} \\ \frac{\partial v^c}{\partial x} \end{Bmatrix}_e = \begin{bmatrix} \frac{\partial N_1}{\partial x} & 0 & \frac{\partial N_2}{\partial x} & 0 & \frac{\partial N_3}{\partial x} & 0 \\ 0 & \frac{\partial N_1}{\partial y} & 0 & \frac{\partial N_2}{\partial y} & 0 & \frac{\partial N_3}{\partial y} \\ \frac{\partial N_1}{\partial y} & 0 & \frac{\partial N_2}{\partial y} & 0 & \frac{\partial N_3}{\partial y} & 0 \\ 0 & \frac{\partial N_1}{\partial x} & 0 & \frac{\partial N_2}{\partial x} & 0 & \frac{\partial N_3}{\partial x} \end{bmatrix}_e \begin{Bmatrix} U^c_1 \\ V^c_1 \\ U^c_2 \\ V^c_2 \\ U^c_3 \\ V^c_3 \end{Bmatrix}_e . \tag{91}$$

Since linear shape functions are employed, the displacement gradient over each element is constant (see Fig. 14). By making use of a simple averaging technique, the nodal value of the displacement gradient tensor are obtained:

$$\bar{\nabla}_I \mathbf{u}^c = \frac{1}{n_I} \sum_{e=1}^{n_I} \nabla \mathbf{u}^c. \tag{92}$$

where $\bar{\nabla}_I$ stands for the nodal value of gradient and n_I is the number of elements related to node I.
Then, an approximation of exact displacement gradient can be obtained by interpolating the nodal values of displacement gradient:

$$\forall \mathbf{x} \in \Omega^c_e, \quad \nabla^* \mathbf{u}^c(\mathbf{x}) = \sum_I N_I(\mathbf{x}) \bar{\nabla}_I \mathbf{u}^c, \tag{93}$$

where ∇^* indicates the recovery-based gradient, and N_I is the nodal shape function that is being used for displacement interpolation.

Finally, the second displacement gradient can be derived from the recovery-based first displacement gradient field:

$$\forall \mathbf{x} \in \Omega_e^c, \quad \nabla\nabla^* \mathbf{u}^c(\mathbf{x}) = \sum_I \mathbf{B}_I(\mathbf{x}) \bar{\nabla} \mathbf{u}_e^c, \tag{94}$$

where $\mathbf{B}_I$ is a matrix that contains the shape function gradients for node I:

$$\mathbf{B}_I = \begin{bmatrix} \frac{\partial N_I}{\partial x} & 0 & 0 & 0 \\ 0 & \frac{\partial N_I}{\partial y} & 0 & 0 \\ \frac{\partial N_I}{\partial y} & 0 & 0 & 0 \\ 0 & 0 & \frac{\partial N_I}{\partial x} & 0 \\ 0 & \frac{\partial N_I}{\partial x} & 0 & 0 \\ 0 & 0 & 0 & \frac{\partial N_I}{\partial y} \\ 0 & 0 & \frac{\partial N_I}{\partial y} & 0 \\ 0 & 0 & 0 & \frac{\partial N_I}{\partial x} \end{bmatrix}, \tag{95}$$

and consequently, the second gradient tensor is given in vector form:

$$\nabla\nabla^* \mathbf{u}^c(\mathbf{x}) = \left[\frac{\partial^2 u}{\partial x^2}, \quad \frac{\partial^2 v}{\partial y^2}, \quad \frac{\partial^2 u}{\partial x \partial y}, \quad \frac{\partial^2 u}{\partial y \partial x}, \quad \frac{\partial^2 v}{\partial x \partial y}, \quad \frac{\partial^2 v}{\partial y \partial x}, \quad \frac{\partial^2 u}{\partial y^2}, \quad \frac{\partial^2 v}{\partial x^2} \right]^T \tag{96}$$

At the end, the norm of second displacement gradient for each element is approximated by the square root of the inner product of $\nabla\nabla^* \mathbf{u}^c(\mathbf{x})$

$$\|\nabla\nabla \mathbf{u}^c\| = \sqrt{\nabla\nabla \mathbf{u}^c \vdots \nabla\nabla \mathbf{u}^c} \simeq \sqrt{(\nabla\nabla^* \mathbf{u}^c)^T \nabla\nabla^* \mathbf{u}^c} \tag{97}$$

In Figure 14, the evaluation of the second displacement gradient $\dfrac{\mathrm{d}^2 u}{\mathrm{d}x^2}$, corresponding to a linear interpolation of u, is depicted for a one-dimensional problem.

4.3. Zienkiewicz-Zhu error estimation

In order to control discretisation error at the coarse scale a simple recovery-based error estimator, proposed by [68], is employed. The Zienkiewicz-Zhu (ZZ) technique is chosen since it is a computationally cheap *a posteriori* error estimator that can easily be incorporated into existing finite element codes. In the ZZ approach, to calculate the error, an approximation for the exact solution is determined by using an averaging technique. After solving finite element problems, a point-wise definition of strain and stress errors at the coarse scale point $\mathbf{x} \in \Gamma^c$ are given by

$$\mathbf{e}_\varepsilon(\mathbf{x}) = \boldsymbol{\varepsilon}^*(\mathbf{x}) - \boldsymbol{\varepsilon}^c(\mathbf{x}) \,, \tag{98}$$

$$\mathbf{e}_\sigma(\mathbf{x}) = \boldsymbol{\sigma}^*(\mathbf{x}) - \boldsymbol{\sigma}^c(\mathbf{x}) \,, \tag{99}$$

where $\mathbf{e}_\varepsilon$ and $\mathbf{e}_\sigma$ are the approximated error in the strain and stress fields, respectively, and $\boldsymbol{\varepsilon}^c$ and $\boldsymbol{\sigma}^c$ are the strain and stress obtained from the finite element solution at the coarse scale. $\boldsymbol{\varepsilon}^*$ and $\boldsymbol{\sigma}^*$ are the approximations of the exact strain and stress which are obtained by interpolating over the nodal values of strain and stress:

$$\forall \mathbf{x} \in \Omega_e, \quad \boldsymbol{\varepsilon}^*(\mathbf{x}) = \mathbf{N}_e(\mathbf{x}) \bar{\boldsymbol{\varepsilon}}_e, \tag{100}$$

$$\forall \mathbf{x} \in \Omega_e, \quad \boldsymbol{\sigma}^*(\mathbf{x}) = \mathbf{N}_e(\mathbf{x}) \bar{\boldsymbol{\sigma}}_e, \tag{101}$$

where $\mathbf{N}_e$ is the matrix of shape functions for the coarse element e, and the nodal averages of stress and strain are denoted by $\bar{\boldsymbol{\sigma}}_e$ and $\bar{\boldsymbol{\varepsilon}}_e$ for the nodes of element e. In order to determine the nodal values of stress $\bar{\boldsymbol{\sigma}}$ and strain $\bar{\boldsymbol{\varepsilon}}$ several methods have been proposed in literature [69, 10, 67]. In this paper, a simple averaging

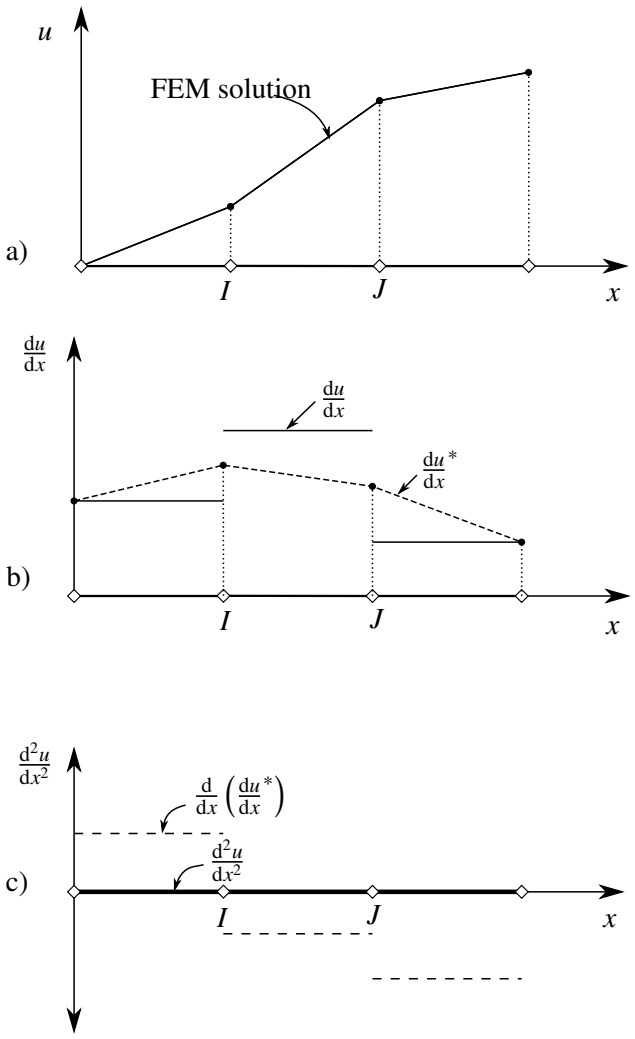

Figure 14: First displacement gradient, $\nabla\mathbf{u}$, second displacement gradient, $\nabla\nabla\mathbf{u}$, and the recovery-based second displacement gradient, $\nabla\nabla^{*}\mathbf{u}$, for a one-dimensional problem and linear shape functions.

technique is used to obtain the nodal value of stress and strain. For example, nodal stress $\bar{\boldsymbol{\sigma}}_I$ at node I is obtained by averaging the stress over all corresponding elements:

$$\bar{\boldsymbol{\sigma}}_I = \frac{1}{n_I} \sum_{e=1}^{n_I} \boldsymbol{\sigma}_e^c. \tag{102}$$

Finally the energy norm of the error for the coarse domain is given by:

$$\forall e \in \Omega^c, \quad \|\mathbf{e}\| = \left(\sum_e \|\mathbf{e}\|_e^2 \right)^{\frac{1}{2}}, \tag{103}$$

where the energy norm of the error for element e is determined by

$$\|\mathbf{e}\|_e^2 = \int_{\Omega_e^c} \mathbf{e}_\sigma^T \mathbf{e}_\varepsilon \, \mathrm{d}\Omega \tag{104}$$

where $\mathbf{e}_\varepsilon$ and $\mathbf{e}_\sigma$ are defined in Eqs. (98) and (99), respectively.
The energy norm of error $\|\mathbf{e}\|$ is normalised by a weighted energy of the system to obtain the relative percentage error η:

$$\eta = \frac{\|\mathbf{e}\|}{\sqrt{\|\mathbf{u}\|^2 + \|\mathbf{e}\|^2}} \times 100\%, \tag{105}$$

where the weighted energy of the system is given by:

$$\|\mathbf{u}\| = \left(\int_{\Omega^c} \boldsymbol{\sigma}^{*T} \boldsymbol{\varepsilon}^* \, \mathrm{d}\Omega \right)^{\frac{1}{2}}. \tag{106}$$

A maximum permissible error $\bar{\eta}$ is defined, and the following condition is checked after each time step:

$$\eta \leq \bar{\eta}. \tag{107}$$

If the condition above is satisfied, the next time step can be started, otherwise, a mesh refinement procedure is triggered.

4.4. Coarse mesh refinement procedure

After convergence of the hybrid multiscale problem at each time step, the ZZ approach is used to measure the energy norm of the error at the coarse mesh. If the inequality (107) is not satisfied one must determine which elements to refine. According to the ZZ procedure, the following inequality

$$\frac{\|\mathbf{e}\|_e}{\bar{e}_m} > 1, \tag{108}$$

defines the coarse elements which are to be refined, where $\|\mathbf{e}\|_i$ is defined in Eq. (104), and

$$\bar{e}_m = \bar{\eta} \left(\frac{\|\mathbf{u}\|^2 + \|\mathbf{e}\|^2}{m} \right)^{\frac{1}{2}} \tag{109}$$

and m is the number of coarse elements. The elements which satisfy (108) are refined by splitting into four smaller elements. In order to have a compatible mesh, the adjacent elements are also split. In Fig. 15, the coarse mesh refinement is depicted. In the adaptive multiscale method after each mesh refinement some modification is required before starting a new time step:

- RVEs corresponding to the parent elements are copied to the new, finer elements,

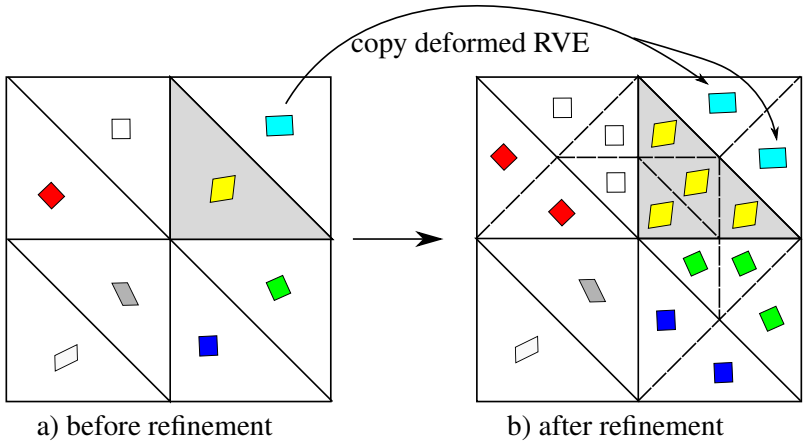

Figure 15: Coarse mesh refinement in FE^2 method, and copying the RVEs from old mesh to the new mesh. An edge bisection method is used. The deformed quadrilaterals represents the underlying RVE corresponding to each coarse element.

- matrix $\mathbf{A}_c$ used in Eq. (83) must be recomputed in order to be compatible with the new configuration of nodes on the interface of coarse-fine meshes.
- the homogenisation error is computed and the scale adaptation condition (90) is checked.
  - if $e_h \leq e_h^{\text{crit}}$ the microstructure adaptation is bypassed,
  - if $e_h > e_h^{\text{crit}}$ the coarse element i is replaced by an explicit representation of the microstrcuture. The adaptation of fully resolved regions is explained in the next section.
- after mesh refinement or microstructure adaptation the residual force will be out of balance due to disturbances in the internal force. Thus, a relaxation procedure is required to minimise the residual force before starting the next time step. See Section 4.7.

4.5. Adaptive expansion of fully resolved region

The fully resolved regions are adaptively expanded to the new critical zones where the coarse elements have a modeling error $e_h > e_h^{\text{crit}}$ or when their corresponding RVEs have already lost the stability. Figure 16 demonstrates the procedure of the development of a fully resolved region schematically. The procedure is slightly different for the initiation of a fully resolved region than the extension of it. A five-step zoom-in procedure can be employed for the extension of an existing fully resolved region (the right column in Fig. 16), while the third step can be skipped for the initiation of the fully resolved region (the left column in Fig. 16).

A zoom-in procedure is started when a critical zone appears at the coarse scale due to the high homogenisation error. The underlying microstructre of the critical zone is determined by opening a window to the actual microstructure. It is assumed that the actual geometry of the microstructure is known *a priori*. In the third step, if the new critical zone is an extension to an existing fully resolved region, then those grains that are common between the existing fully resolved region and its extension are attached to the extension part, and all related data are dismissed. In the fourth step, the extension part is meshed in such a way that the mesh is compatible with the adjacent coarse mesh and fully matches with the adjacent fully resolved regions. The fourth step also consists of an equalisation process that solves the new fully resolved region boundary value problem based on the history of displacement field that has been experienced by the critical zone. Equalisation process is detailed in Section 4.6. At the end of equalisation process, the displacement field of the new fully resolved region is compatible with the surrounding meshes, and the level of energy saved in the high resolution region is approximately equal to the amount of strain energy in the coarse elements before adaptation. The equalisation process will be explained in the next section. In the next step,

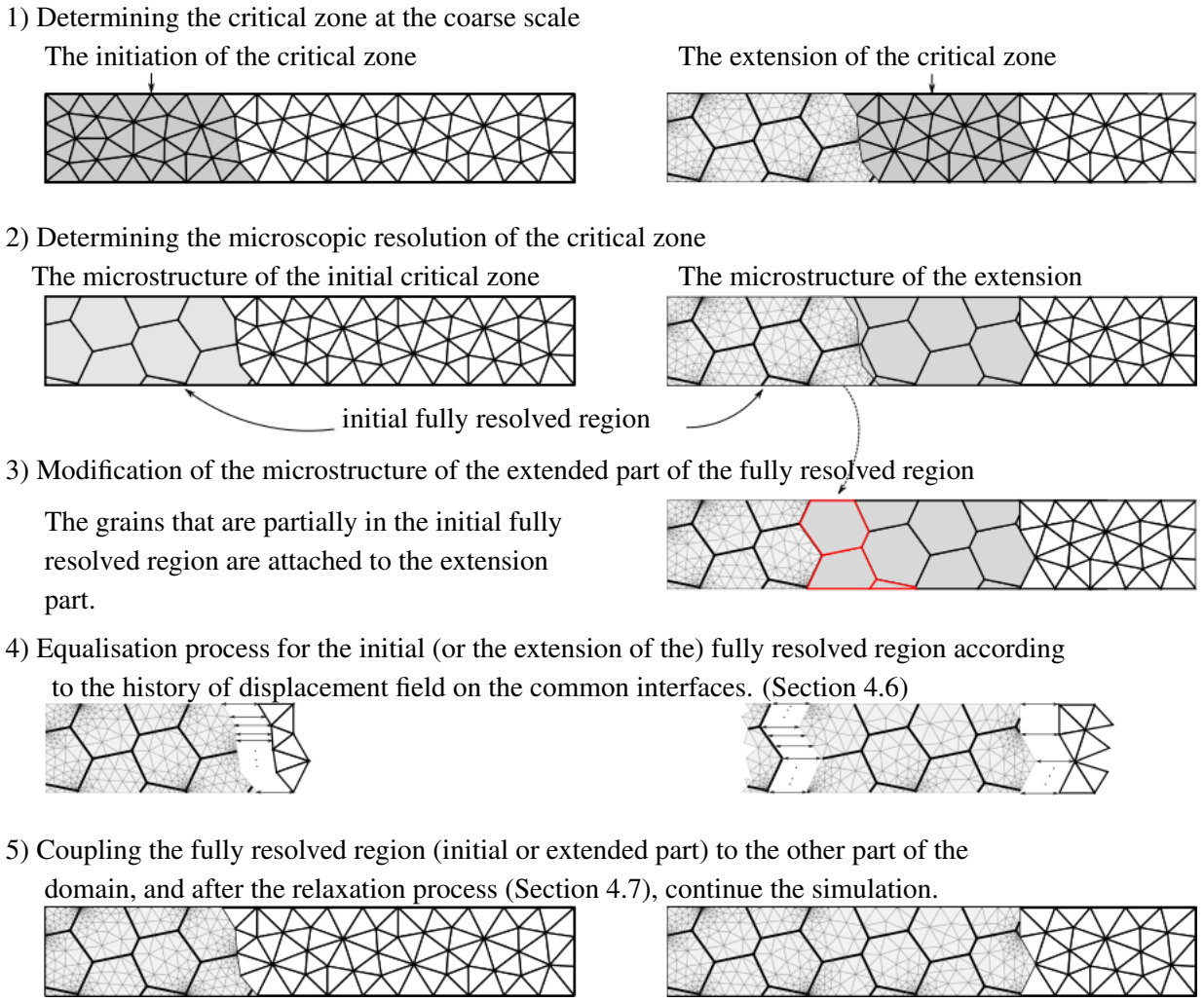

Figure 16: The procedure of the development of the fully resolved region

the Linear Multiple Point Constraint (LMPC) technique is used to couple the the new fully resolved region to the rest of the domain. Finally, before continuing the simulation, a relaxation procedure is performed to minimise the out-of-balance residual force as described in Section 4.7.

4.6. Equalisation process

When the critical coarse elements are replaced by a fully resolved region, it is necessary to ensure that the high resolution region and critical coarse elements have equivalent strain energy and deformation states. In our problem, the two physical models are equivalent if the level of damage, or more precisely, their capacity to store strain energy with the same deformed shape, are equal. The undamaged microstructure saves more strain energy rather than the coarse scale critical zone due to its un-degraded stiffness. The equalisation process is performed to acquire an approximately equivalent fully resolved region. In the equalisation process, a BVP is defined for the undamaged high resolution domain. The boundary conditions are defined from the displacements experienced by the critical zone during the simulation up until the current time step ($t \in [0, \tau]$). Figure 17 illustrates equalisation process for a fully resolved region based on the displacement history of the critical zone. For linear elastic microstructures, the whole history of displacement can be imposed by a single time step only since the material capacity for storing strain energy is not changed by loading. Similar to Section 3.4, the LMPC method is adopted to impose the displacement boundary conditions. At this stage, no arc-length technique is required since the external load (displacement history) is

known for all previous time steps. After accomplishment of the equalisation process, the fully resolved region is embedded into the coarse scale by making use of the LMPC technique. The coupling technique between the fine and the coarse meshes was explained in Section, 3.4.

4.7. Relaxation

After the equalisation process, the embedding of the fully resolved region into the coarse scale, and before starting the new time step, the residual force vector must again be minimised. After every mesh refinement or adaptation of the high resolution scale, the internal forces change. Therefore, the simulation is continued at the current time step until the norm of the residual force vector reduced to a certain acceptable tolerance.

5. Local Arc-length technique

When a cohesive interface fails, two operations are performed simultaneously: the traction at the cohesive interface decreases, and the elastic grains unload. Because the grains are elastic and cohesive crack failure is not ductile, the energy released by unloaded grains provides more energy than necessary for the cohesive crack growth. Also due to the unloading in the elastic region a snap-back behaviour is expected. Therefore, an equilibrium state cannot be found for either an increment of external load or an increment of applied displacement boundary condition (see Fig. 18). In another words, load incremental strategy and displacement incremental strategy are not able to trace the solution path in the snap-back regime. The arc-length method is a numerical procedure that is used to follow the solution path in nonlinear problems. This method was originally proposed by [66] and [53], developed by [14] and later modified by several researchers. In the arc-length method, a continuous path of equilibrium can be traced by considering a feasible constraint equation. The constraint equation adds one unknown variable and one equation to the nonlinear system of equations. Comprehensive reviews of several arc-length methods can be found in [15, 21]. Two classes of arc-length methods exist. The first group contains global arc-length techniques which define a constraint over the whole of the solution space and can follow smooth load-displacement curves [14, 45]. The second group are called local arc-length methods. They impose a constraint equation on a local region and can trace nonlinear solutions with very sharp snap-back [55, 5].

In this work, when a fully resolved region occurs in the simulated structure, the incremental force procedure is switched to a local arc-length procedure. In this local arc-length method, a constraint equation is introduced so that at each time step, the maximum local increment in the displacement jump $\Delta[\![\mathbf{u}^f]\!](\zeta_{\mathrm{m}})$ over the mid-point ζ_{m} of all the cohesive elements (whose stiffness is positive) takes a predefined value Δl over the current time step $[t,\ t+\Delta t]$:

$$\forall e \in \Gamma^f, \quad \mathbf{P}_e\ \Delta[\![\mathbf{u}^f_m]\!]_e \leq \Delta l, \tag{110}$$

where e refers to the cohesive elements on the cohesive interface Γ^f, and $\mathbf{P}_e = \dfrac{[\![\mathbf{u}^f]\!]_e^T}{\|[\![\mathbf{u}^f]\!]_e\|}$ is the jump direction of the cohesive element e at the last time step $[t-\Delta t,\ t]$. More detail can be seen in Fig. 19.

To control the external load at the coarse scale, this constraint is defined at the fine scale and linked to an unknown parameter γ which is the amplitude of the external load $\mathbf{F}$. The constraint equation (110) is added to the system of equilibrium equations (84), thus the algebraic nonlinear problem to solve, in the concurrent multiscale phase, reads:

$$\begin{cases} \mathbf{R}^c\left(\mathbf{U}^c, \boldsymbol{\lambda}, \gamma\right) = \mathbf{f}^c_{\mathrm{int}}\left(\mathbf{U}^c\right) - \gamma \mathbf{f}^c_{\mathrm{ext}} - \mathbf{A}^{cT}\boldsymbol{\lambda} = \mathbf{0}, \\ \mathbf{R}^f\left(\mathbf{U}^f, \boldsymbol{\lambda}, \gamma\right) = \mathbf{f}^f_{\mathrm{int}}\left(\mathbf{U}^f\right) - \gamma \mathbf{f}^f_{\mathrm{ext}} + \mathbf{A}^{fT}\boldsymbol{\lambda} = \mathbf{0}, \\ \mathbf{R}^\Gamma\left(\mathbf{U}^c, \mathbf{U}^f\right) = \mathbf{A}^f\mathbf{U}^f - \mathbf{A}^c\mathbf{U}^c = \mathbf{0}, \\ \forall e \in \Gamma^f, \quad \mathbf{P}_e\ \mathbf{B}^\Gamma_{e_m}\Delta\mathbf{U}^f_e \leq \Delta l, \end{cases} \tag{111}$$

where $\mathbf{B}^\Gamma_{e_m} = \mathbf{B}^\Gamma_e(\zeta_m)$ is the jump extractor matrix for the mid-point of the cohesive element e that is given by Eq. (32). According to [42], the nonlinear Eqs. (111) can be solved by linearisation of the first three

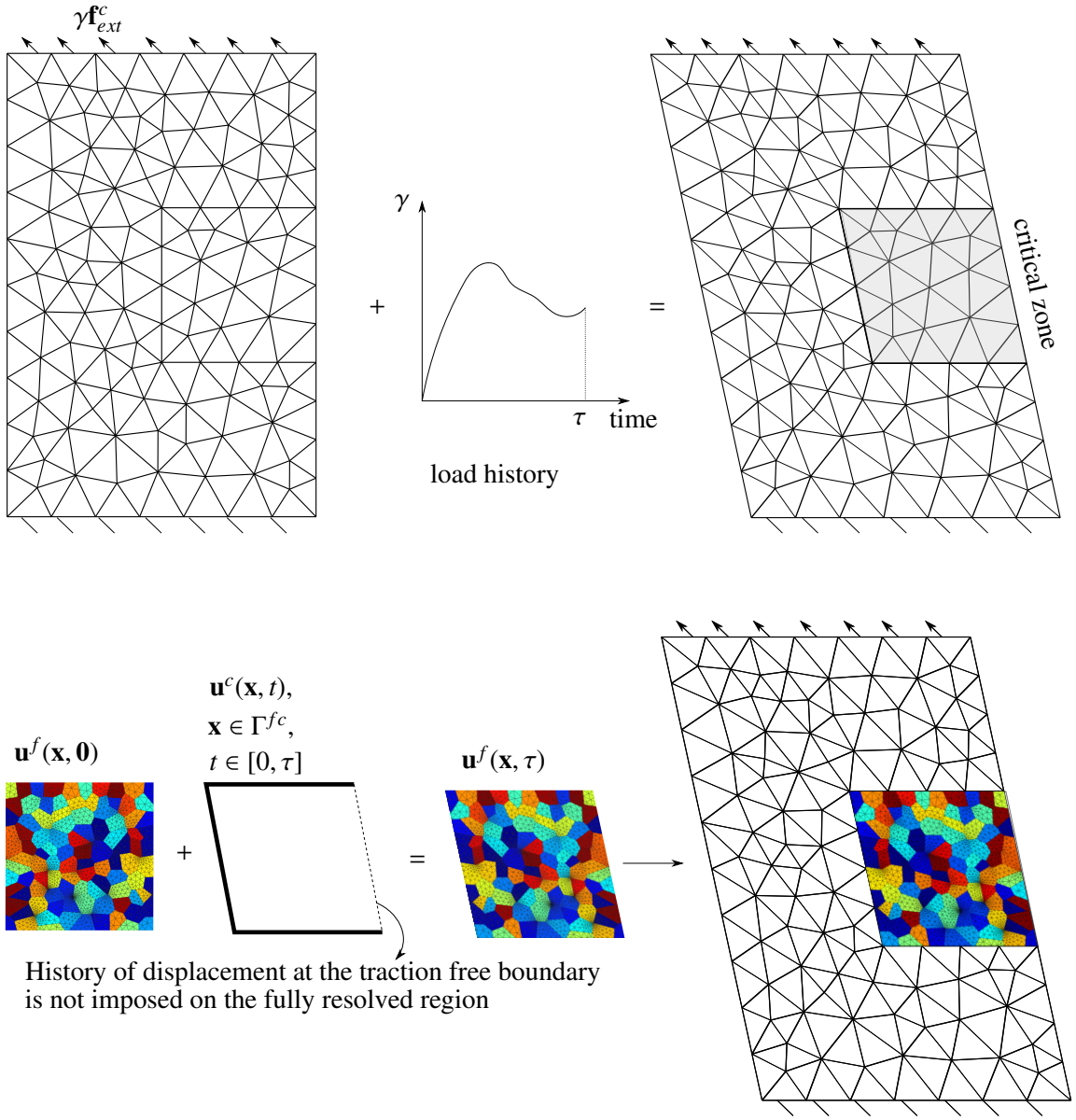

Figure 17: Solving the fully resolved region using a boundary condition based on the displacement history of the corresponding critical zone.

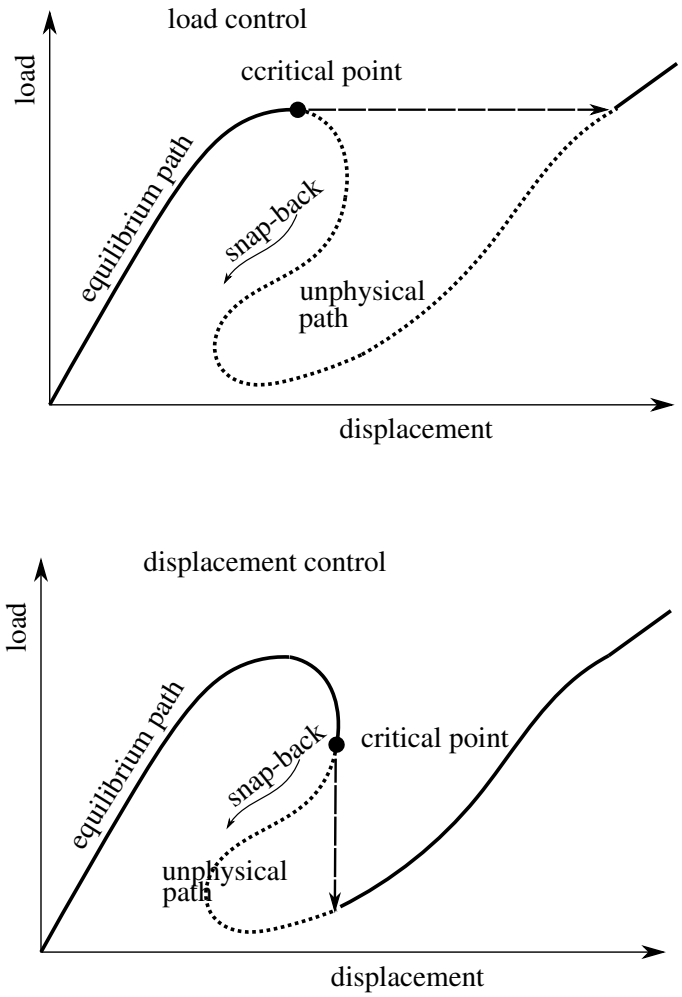

Figure 18: Load-displacement equilibrium obtained by the load control and displacement control procedures. The unphysical equilibrium path, shown by dash-line, cannot be followed by the load control and displacement control procedures.

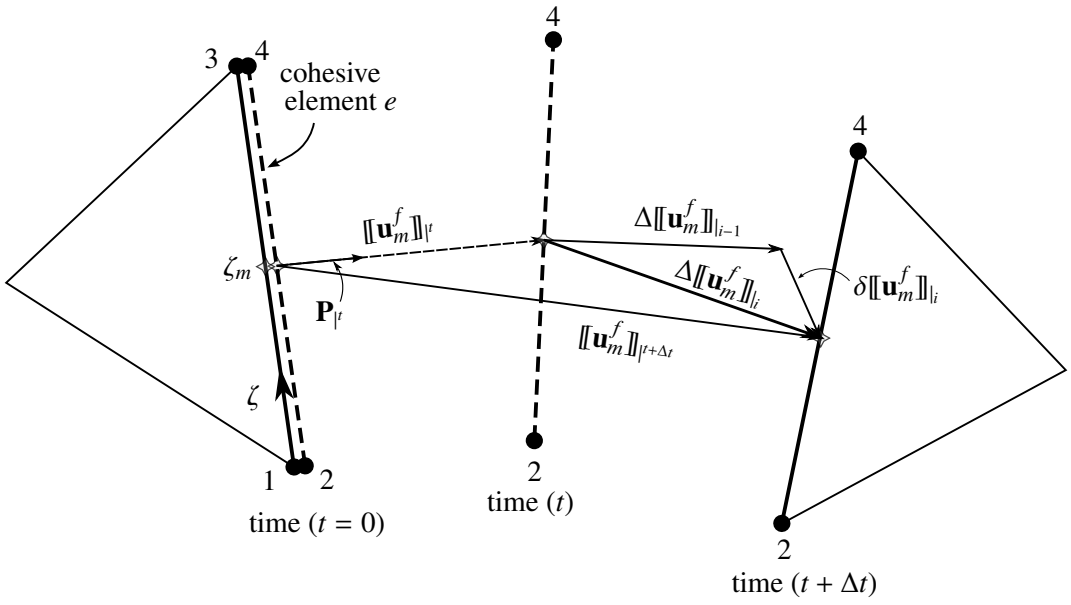

Figure 19: The variation of the displacement jump $[\![\mathbf{u}^f]\!]$ at the middle point ζ_m of cohesive element e

equations, and a direct solution procedure is carried out for the arc-length constraint equation. The linearised form of the equations is given by:

$$\begin{bmatrix} \mathbf{K}_T^c & \mathbf{0} & -p\mathbf{A}^{cT} \\ \mathbf{0} & \mathbf{K}_T^f & p\mathbf{A}^{fT} \\ -p\mathbf{A}^c & p\mathbf{A}^f & \mathbf{0} \end{bmatrix} \begin{Bmatrix} \delta\mathbf{U}^c \\ \delta\mathbf{U}^f \\ \delta\bar{\boldsymbol{\lambda}} \end{Bmatrix} = -\begin{Bmatrix} \mathbf{R}^c \\ \mathbf{R}^f \\ \mathbf{R}^\Gamma \end{Bmatrix} + \begin{Bmatrix} \mathbf{f}_{\text{ext}}^c \\ \mathbf{f}_{\text{ext}}^f \\ \mathbf{0} \end{Bmatrix} \delta\gamma. \tag{112}$$

Lagrange multipliers $\boldsymbol{\lambda}$ are replaced by $p\bar{\boldsymbol{\lambda}}$ to avoid the conditioning number of the system of equations being affected by the heterogeneity of the unknown vector. p was introduced in Eq. (86). Eq. (112) cannot be solved, Because $\delta\gamma$ is unknown, however a relationship between unknown vector on LHS and $\delta\gamma$ can be found:

$$\begin{Bmatrix} \delta\mathbf{U}^c \\ \delta\mathbf{U}^f \\ \delta\bar{\boldsymbol{\lambda}} \end{Bmatrix} = -\begin{Bmatrix} \mathbf{a}^c \\ \mathbf{a}^f \\ \mathbf{a}^\Gamma \end{Bmatrix} + \begin{Bmatrix} \mathbf{b}^c \\ \mathbf{b}^f \\ \mathbf{b}^\Gamma \end{Bmatrix} \delta\gamma, \tag{113}$$

where

$$\begin{Bmatrix} \mathbf{a}^c \\ \mathbf{a}^f \\ \mathbf{a}^\Gamma \end{Bmatrix} = \begin{bmatrix} \mathbf{K}_T^c & \mathbf{0} & -p\mathbf{A}^{cT} \\ \mathbf{0} & \mathbf{K}_T^f & p\mathbf{A}^{fT} \\ -p\mathbf{A}^c & p\mathbf{A}^f & \mathbf{0} \end{bmatrix}^{-1} \begin{Bmatrix} \mathbf{R}^c \\ \mathbf{R}^f \\ \mathbf{R}^\Gamma \end{Bmatrix}, \tag{114}$$

and

$$\begin{Bmatrix} \mathbf{b}^c \\ \mathbf{b}^f \\ \mathbf{b}^\Gamma \end{Bmatrix} = \begin{bmatrix} \mathbf{K}_T^c & \mathbf{0} & -p\mathbf{A}^{cT} \\ \mathbf{0} & \mathbf{K}_T^f & p\mathbf{A}^{fT} \\ -p\mathbf{A}^c & p\mathbf{A}^f & \mathbf{0} \end{bmatrix}^{-1} \begin{Bmatrix} \mathbf{f}_{\text{ext}}^c \\ \mathbf{f}_{\text{ext}}^f \\ \mathbf{0} \end{Bmatrix}. \tag{115}$$

In order to obtain $\delta\gamma$, the middle line of Eq.(113), $\delta\mathbf{U}^f = -\mathbf{a}^f + \mathbf{b}^f\delta\gamma$, is substituted into the arc-length constraint equation (111):

$$\forall e \in \Gamma^f, \quad \mathbf{P}_e\mathbf{B}_{e_m}^\Gamma \overbrace{\left(\Delta\mathbf{U}_{e\,|_{i-1}}^f - \mathbf{a}^f + \mathbf{b}^f\delta\gamma\right)}^{\Delta\mathbf{U}_{e\,|_i}^f} \leq \Delta l, \tag{116}$$

where at each time step, $\Delta\mathbf{U}^f{}_{|_i} = \Delta\mathbf{U}^f{}_{|_{i-1}} + \delta\mathbf{U}^f{}_{|_i}$ is the total variation of displacement, and $\delta\mathbf{U}^f{}_{|_i}$ is the variation of displacement at the current iteration $|_i$ which was replaced by $-\mathbf{a}^f + \mathbf{b}^f\delta\gamma$ according to Eq. 113. Rearranging Eq. (116):

$$\forall e \in \Gamma^f, \quad f_e(\delta\gamma) = \mathbf{P}_e\mathbf{B}_{e_m}^\Gamma\left(\Delta\mathbf{U}_{e\,|_{i-1}}^f - \mathbf{a}^f\right) + \mathbf{P}_e\mathbf{B}_{e_m}^\Gamma\mathbf{b}^f\delta\gamma \leq \Delta l, \tag{117}$$

where $f_e(\delta\gamma)$ is a linear equation in $\delta\gamma$ which will always yield a value of $\delta\gamma$ that satisfies $f_e(\delta\gamma_e) = \Delta l$. Therefore, for each cohesive element e an admissible domain S_e exists such that:

$$S_e = \{\delta\gamma | \delta\gamma \in \mathbb{R},\ f_e(\delta\gamma) \leq \Delta l\}. \tag{118}$$

Finally, the common interval between all admissible intervals S provides an admissible interval S_a for all the cohesive elements which have not been fully damaged:

$$\forall e \in \Gamma^f, \text{ and } d_e(\zeta_m) < 1, \quad S_a = [\delta\gamma_l,\ \delta\gamma_r] = \bigcap^e S_e. \tag{119}$$

where $\delta\gamma_l$ and $\delta\gamma_r$ are the minimum and maximum values of the admissible interval S_a. In fact, the variation of the jump in fully opened cohesive cracks (dead cracks) is not controlled, so their admissible intervals are not considered when determining the global admissible interval S_a. A schematic for the evaluation of the admissible interval of $\delta\gamma$ for all cohesive elements is given in Figure 20. However, it is possible that a common interval cannot be found for all active cohesive elements, in which case, this time step is repeated

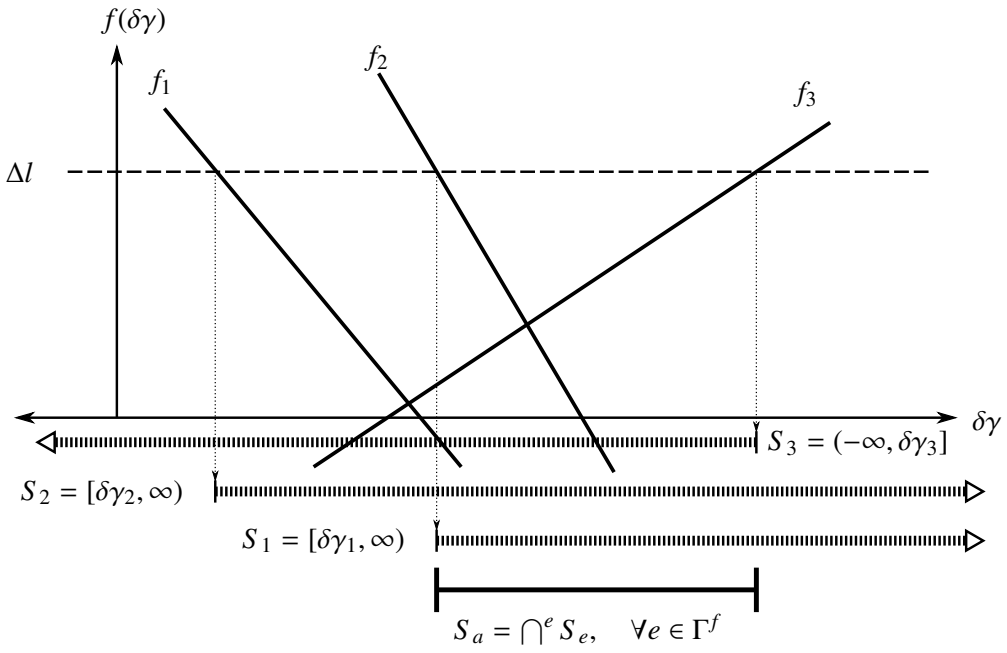

Figure 20: The evaluation of the admissible interval S_a for the variational load factor $\delta\gamma$ in the local arc-length method.

Table 1: Material properties and parameters for grain and cohesive interfaces at the microscale.

grain			cohesive interface			
E	ν	l_g	$\sigma_{\max} = \tau_{\max}$	$G_{Ic} = G_{IIc}$	κ_{ini}	n
384.6GPa	0.237	25μm	1 GPa	35 Jm^{-2}	0	0.5

with a slightly different (larger/smaller) value of Δl. A bound for Δl must be considered to avoid very large jumps at cohesive interfaces. Based on the critical displacement jump of cohesive interfaces $[\![\mathbf{u}]\!]_{\text{full}}$ (see Eq. (17)), a bound for the maximum variation of displacement jump is determined:

$$0.01[\![\mathbf{u}]\!]_{\text{full}} < \Delta l < [\![\mathbf{u}]\!]_{\text{full}} \tag{120}$$

In this local arc-length method, an admissible interval for $[\delta\gamma_l,\ \delta\gamma_r]$ is determined, but the value of $\delta\gamma \in [\delta\gamma_l,\ \delta\gamma_r]$ which minimises the residuals in Eq. (111) remains unknown. In this work, the maximum variation of load factor $\delta\gamma_r$ is chosen which maximises the load factor γ.

6. Example Applications

In this section, the proposed adaptive multiscale method for polycrystalline failure presented is tested. A notched beam under uni-axial load is considered as a test case for the adaptive multiscale method. A direct numerical solution (DNS) where the whole microstructure is explicitly simulated over the whole computational domain for comparison of the results.

6.1. Notched Beam

As an example, a single-notched beam under uniaxial load is considered, shown in Fig. 21. The results from the proposed multiscale framework are compared to those from a direct numerical solution (DNS). The beam is made of a polycrystalline material, for which the constitutive equations were introduced in Section **??**, and the mechanical properties of the grains are given in Table 1. In order to decrease the computational cost, the FE^2 method is only implemented in the middle part of the beam (grey region in Fig. 21), and

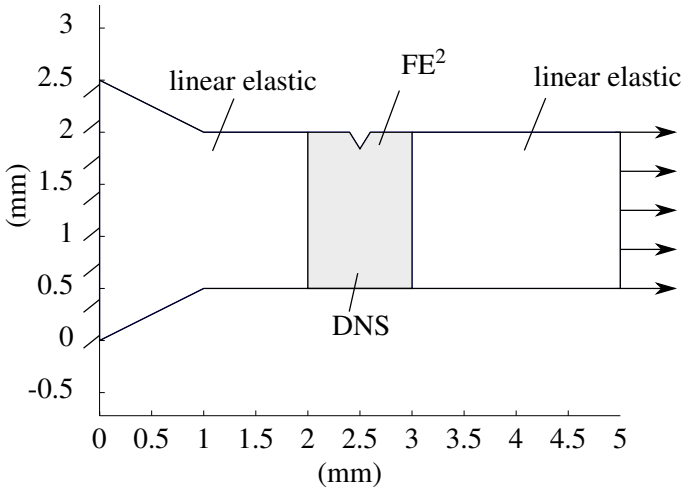

Figure 21: A single-notched beam under uniaxial tensile load.

a constant linear elastic homogenised model with Young's modulus $E = 386.4$ GPa and Poisson's Ratio $\nu = 0.237$ is considered for the rest of the domain. Furthermore, for the DNS problem, only the middle region is resolved at the microscale. Distribution of the von Mises stress over the notched beam are shown

in Fig. 22 for the DNS and the adaptive multiscale solution.

As explained in Section 4, the ZZ error estimator is employed for the control of the discretisation error, and the strain-gradient sensitivity is used as a measurement for the homogenisation error. The maximum permissible discretisation error is $\bar{\eta} = 5\%$. If the strain-gradient sensitivity of a coarse element $L_{\mathcal{V}}\|\nabla\nabla\mathbf{u}^c\|_e$ is higher than the critical value of the homogenisation error then the microstructure is fully resolved for that element. In this study, $e_h^{\text{crit}} = 0.01$ is considered as the critical value of homogenisation error. The distribution of the strain-gradient sensitivity of the coarse mesh is illustrated in Fig. 23. It is observed that the mostly the coarse elements in the vicinity of the crack tip have the high strain-gradient sensitivity. As shown in this figure, this homogenisation error indicator can accurately predict the most likely direction of the crack propagation, which is the main advantage of this scale adaptation criterion. In the literature, the length scale ratio [62, 24] have been used as the scale adaptation criterion in multiscale fracture modelling. This usually lead to a large fully resolved region at the coarse scale. In scale adaptation based on the length scale ratio, if the ratio of the coarse element size to the RVE size is less than a critical value, then the microstrucute is directly resolved at those elements.

In Fig. 24, the coarse mesh in the vicinity of the fully resolved region is shown. Although some coarse elements are smaller than the size of a grain, which means that they are at the same scale, according to the homogenisation error criterion, it is still allowed to use the FE^2 method. It is worth to mention that, if scale size ratio was used as scale adaptation criterion, the most of these coarse elements in the vicinity of the microscopic region must be fully resolved at the microscale, while the strain-gradient sensitivity of those elements is still less that the critical value $e_h^{\text{crit}} = 0.01$.

For the notched beam, the variation of the external work W_{ext}, total strain energy W_{int}, and the dissipated energy D versus the time steps are shown in Fig. 25. The beam reaches its maximum strain energy at time step 8. In the next time steps, the arc-length method decreases the external load in order to track the snap-back behaviour of the load-displacement curve, and therefore, the level of the external work and the strain energy of the beam drop dramatically (Time step 15). In this stage, the grains around the notch are separated, and a macro-crack is nucleated. Although the strain energy and the external work show oscillation, the dissipated energy of the beam is monotonically increasing. This is because the local arc-length enforces the cohesive cracks to dissipate energy at each time step according to the constraint equation (110). Therefore, even if the external load decreases at least one of the cohesive cracks dissipates energy.

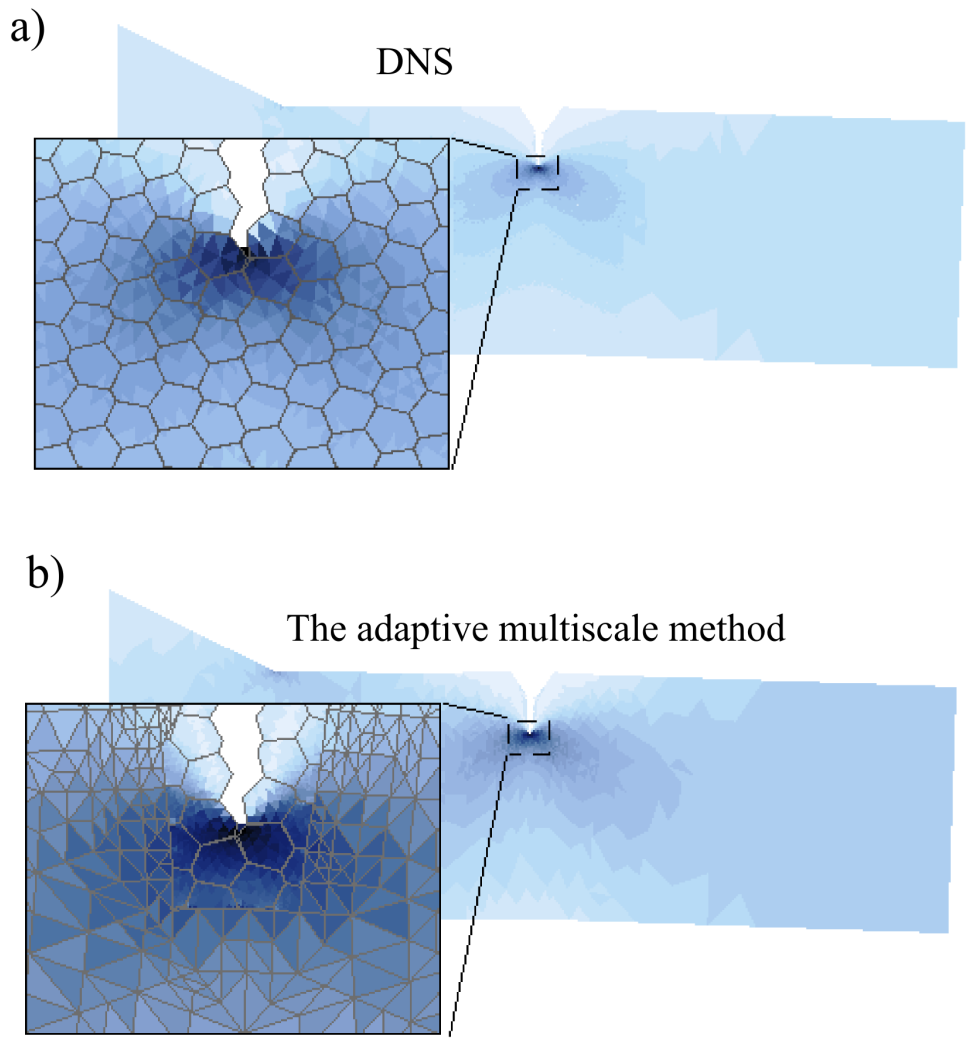

Figure 22: von Mises stress distribution in the notched bar a) DNS, b) Adaptive multiscale solution. Deformation is magnified by 100.

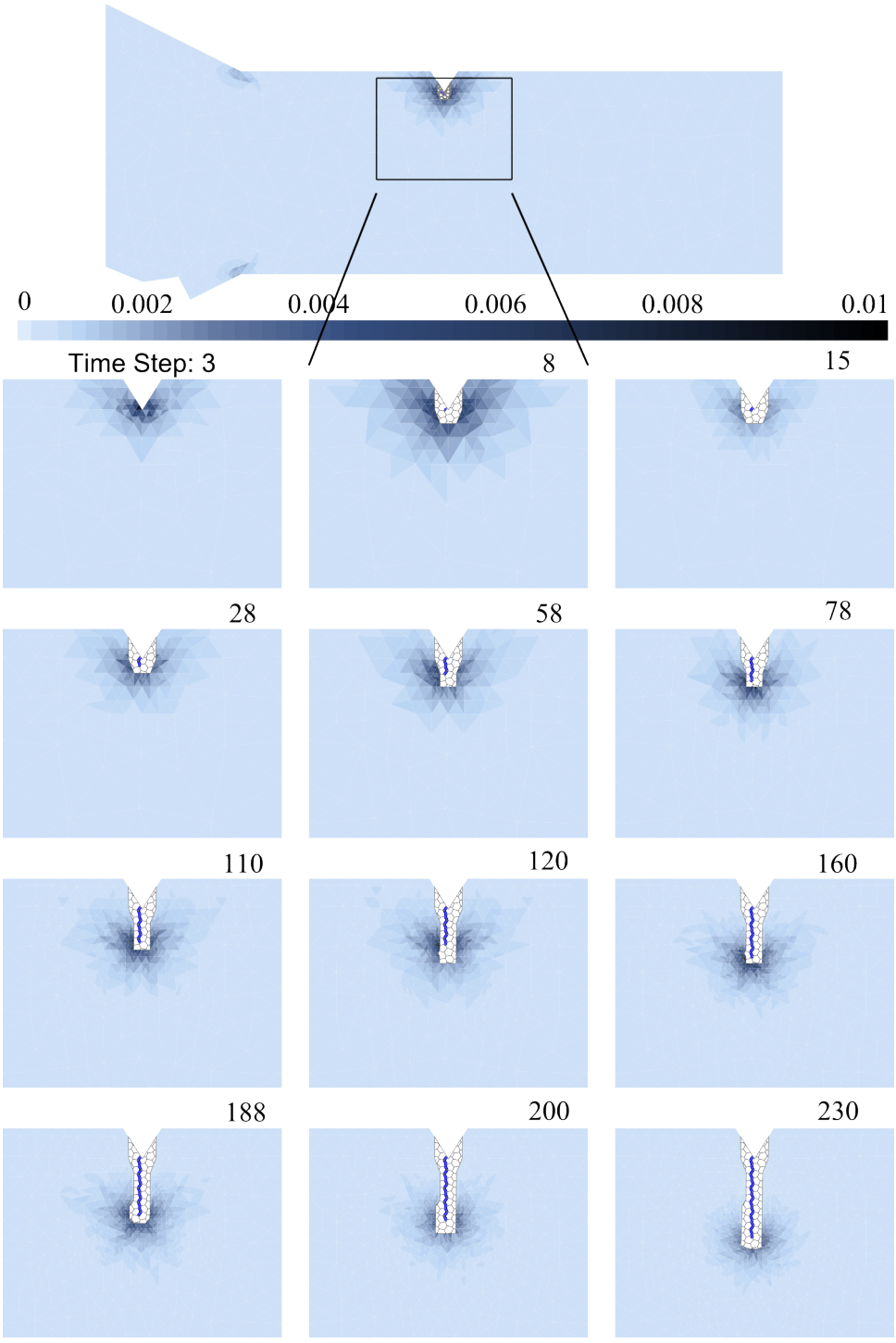

Figure 23: The distribution of strain-gradient sensitivity $L_{\mathcal{V}}\|\nabla\nabla\mathbf{u}^c\|_e$ at the coarse scale, and the adaptive development of the fully resolved region.

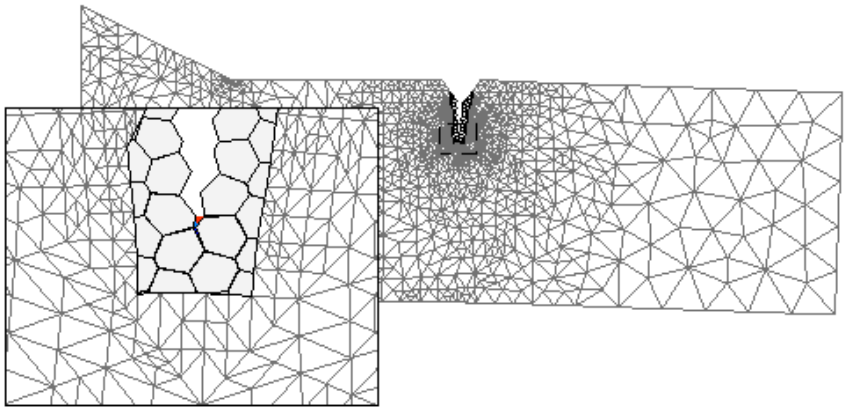

Figure 24: Coarse mesh in the adaptive multiscale at Time step 200. Deformation is magnified by 100.

The external work W_{ext}, the total strain energy W_{int} and the dissipated energy D of the beam at time τ are obtained by the following equations:

$$W_{\text{ext}} = \int_{t=0}^{\tau} \int_{\partial\Omega_N} \mathbf{F} \cdot \Delta\mathbf{u}^{\mathbf{c}}(t)\, \mathrm{d}\Gamma\, \mathrm{d}t, \tag{121}$$

$$W_{\text{int}} = 0.5 \int_{\partial\Omega_N} \mathbf{F} \cdot \mathbf{u}^{\mathbf{c}}(\tau)\, \mathrm{d}\Gamma, \tag{122}$$

$$D = W_{\text{ext}} - W_{\text{int}}, \tag{123}$$

where t is the time, $\Delta\mathbf{u}^{\mathbf{c}}$ is the variation of the macroscopic displacement in each time step, and $\mathbf{F}$ is the external traction load on the Neumann boundary, $\partial\Omega_N$.

In Fig. 26, the deformation of the fully resolved region at two time steps is shown: 1) time step 8 when the domain is experiencing its maximum level of strain energy, and 2) time step 15 when the crack is initiated and the strain energy of the domain drops.

The energy dissipation in the beam versus the displacement at the tip of the beam is shown in Fig. 27. In this figure, the result from the adaptive multiscale method is compared with DNS results. It is observed that the total dissipated energy D obtained from the adaptive multiscale method is less than the dissipated energy from the DNS for the same displacement. As expected, any variation of displacement causes an increase in the total dissipated energy.

In Fig. 28, the dissipated energy in terms of crack length is shown for the adaptive multiscale method and the DNS. In calculating the crack length, the cohesive cracks with the damage parameter d larger than 0.423 is considered as a fully opened crack. This is because the traction-separation law transitions to the softening regime when $d > 1 - (\frac{n}{n+1})^n$. In this study $n = 0.5$ (See Section 2.2). The initially dissipated energy before the macro-crack initiation in the DNS is 10% more than that in the adaptive multiscale method. This is due to the fact that the larger fully resolved region of the DNS allows the damage to diffuse into a wider area, and consequently, dissipates more energy before the crack initiation. In contrast, the adaptive multiscale model dissipates less energy before the macro-crack initiation, because of 1) the small fully resolved region stops the cohesive cracks on the coarse-fine mesh interface Γ^{fc} to dissipate energy before initiation of the first crack, and 2) the coarse elements dissipate less energy due to the small size of the RVE employed for

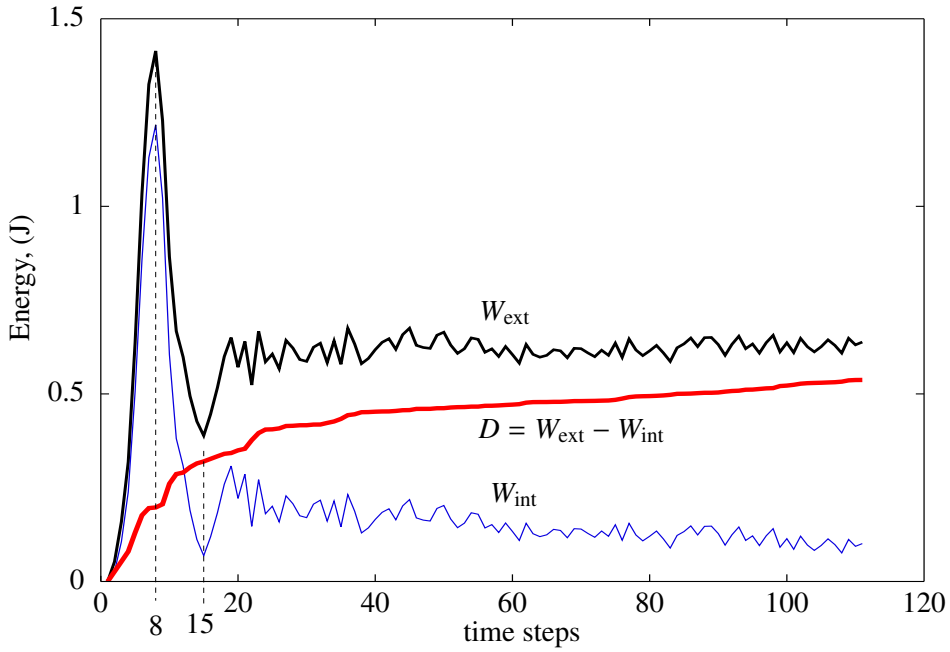

Figure 25: Variation of the external work W_{ext}, the strain energy W_{int}, and the dissipated energy D in a notched beam under a uniaxial load.

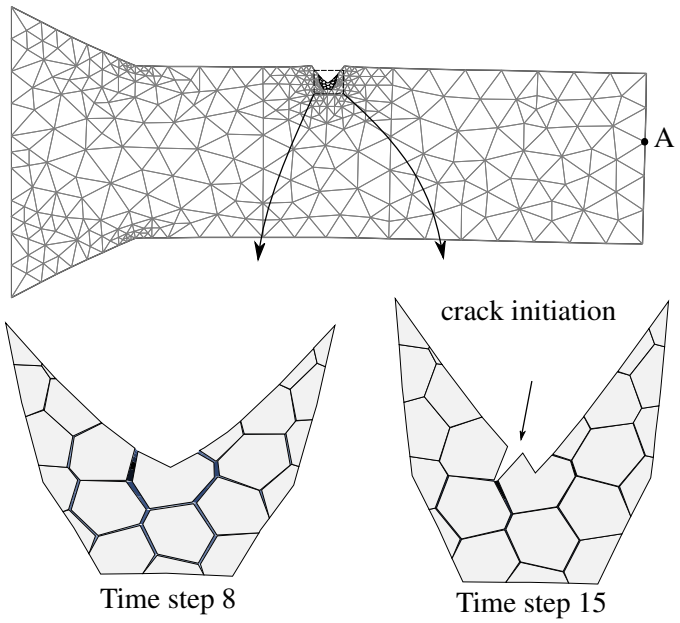

Figure 26: Capturing the crack initiation at the grain scale using adaptive multiscale method. Deformation is magnified by 100.

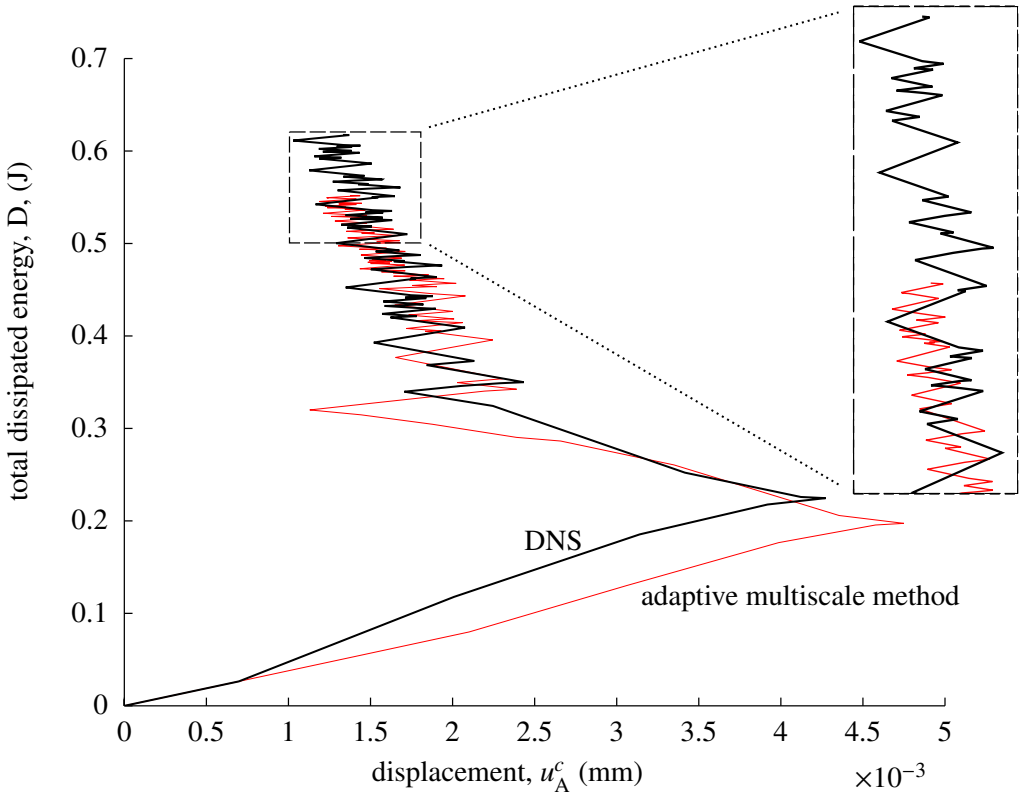

Figure 27: The variation of dissipated energy D versus displacement at the Neumann boundary of notched beam (Point A in Fig. 26).

homogenisation. In addition, the rate of energy dissipation in the DNS is higher than that in the adaptive multiscale method.

The load-displacement curve obtained from the adaptive multiscale method is compared with DNS result in Fig. 29. It is observed that the adaptive multiscale method shows the higher value for the yield strength and stiffness in compare to the DNS. It can be seen that the local arc-length method is able to follow a high oscillatory behaviour of load-displacement curve.

7. Conclusions

For modelling failure in polycrystalline materials, an adaptive multiscale method was developed. A thermodynamically consistent cohesive crack model was implemented to model the interface between the grains, and the grains were modelled as a linear elastic material. The classical homogenisation technique was used to obtain the macroscopic response of the heterogeneous microstructure. The Zienkiewicz-Zhu error estimator was used to control the discretisation error at the coarse scale, and the homogenisation error measurement, devised by [59] was implemented to control the modelling error. When the homogenisation error exceeds a critical value, the corresponding coarse element is replaced by underlying microstructure. This fully resolved region is expanded adaptively in order to control the modelling and discretisation errors that increase due to the crack propagation. To follow the highly non-linear load-displacement curve, a local arc-length technique was developed for the adaptive multiscale framework.

The following contributions were made to the existing computational multiscale techniques for the modelling of fracture in polycrystalline materials

- A robust local arc-length technique was designed for concurrent multiscale methods that can follow sharp snap-back in the load-displacement curve by controlling the opening of cracks at the microscale.

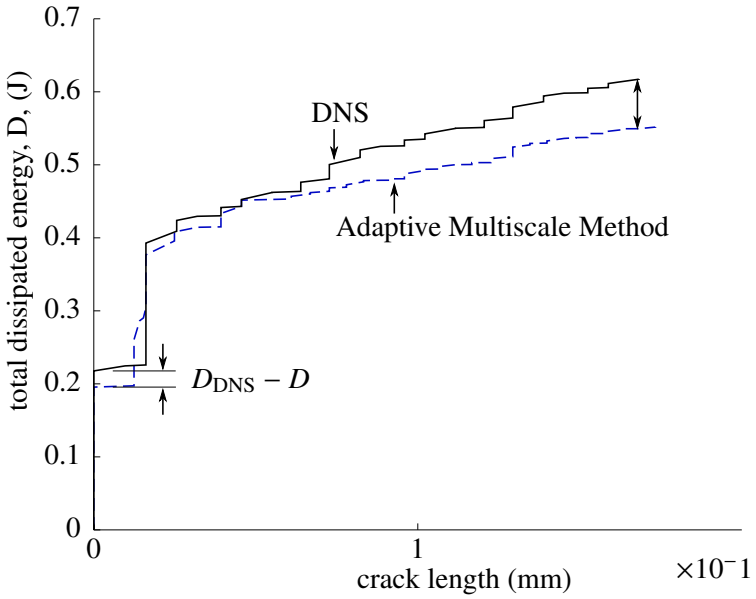

Figure 28: The variation of dissipated energy D versus crack length.

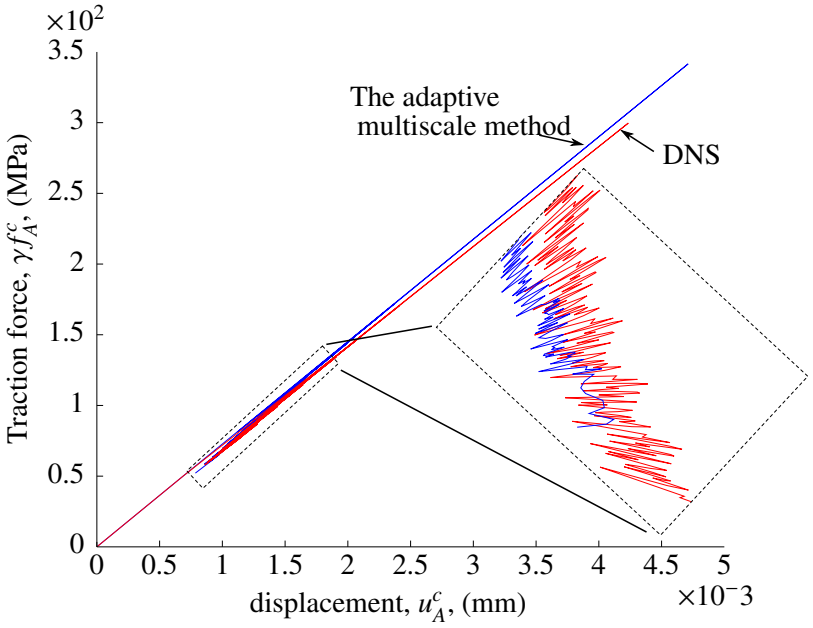

Figure 29: The load-displacement curve for the single notched beam.

- The proposed multiscale method for modelling fracture was equipped with 1) an adaptive unstructured coarse mesh, and 2) a progressive fully resolved region that makes it possible to model crack propagation.

- A procedure was devised that allows to adaptively expand the fully resolved region, which contains nonlinear cohesive cracks, into the coarse scale mesh.

- Discretisation and homogenisation model error estimators were employed to control both the adaptivity of the coarse mesh and the extension of the fully resolved region. The discretisation error at the coarse scale was controlled by the Zienkiewicz-Zhu procedure, and strain-gradient sensitivity was used to measure the homogenisation error. To obtain the second displacement gradient when using triangular linear elements, an averaging technique was proposed to obtain a smoothed field for the first displacement gradient. Then the second displacement gradient with C_0 continuity was obtained from the smoothed field of the first displacement gradient.

- The multiscale method was shown, numerically to produce results which are almost identical to direct numerical simulations.

The fracture of a notched beam under a uniaxial load was modelled by the proposed adaptive multiscale method. According to the results, one can conclude that:

- The strain-gradient sensitivity criterion is able to predict the direction of the crack propagation by defining the critical region for scale adaptation.

- The size of the critical region flagged by the strain-gradient sensitivity is smaller than the size of the critical region flagged by the scale ratio criterion. In other words, it was shown that the FE^2 method can be used for coarse elements that are even smaller than the RVE size if the strain-gradient sensitivity does not exceed its critical value.

- The adaptive multiscale method shows less energy dissipation in comparison to the DNS.

Acknowledgements

[1] Shephard MS. Abel JF. An algorithm for multipoint constraints in finite element analysis. *International Journal for Numerical Methods in Engineering*, 14(3):464–467, 1979.

[2] Mark Ainsworth and J Tinsley Oden. A posteriori error estimation in finite element analysis. *Computer Methods in Applied Mechanics and Engineering*, 142(1-2):1–88, 1997.

[3] M. V. Cid Alfaro, a. S. J. Suiker, C. V. Verhoosel, and R. Borst. Computational homogenization of discrete fracture in fibre-epoxy systems. *International Journal of Material Forming*, 2(S1):931–934, December 2009.

[4] O Allix and A Corigliano. Modeling and simulation of crack propagation in mixed-modes interlaminar fracture specimens. *International Journal of Fracture*, 77(2):111–140, 1996.

[5] O Allix, P Kerfriden, P Gosselet, Lmt-cachan E N S Cachan, Cnrs Upmc, and Pres Universud. On the control of the load increments for a proper description of multiple delamination in a domain decomposition framework . *International Journal for Numerical Methods in Engineering*, 11:1518–1540, 2010.

[6] A Mobasher Amini, D Dureisseix, and P Cartraud. Multi-scale domain decomposition method for large-scale structural analysis with a zooming technique : Application to plate assembly. *International Journal For Numercal Methods In Engineering*, 79(February):417–443, 2009.

[7] Christine Bernardi, Yvon Maday, and Francesca Rapetti. Basics and some applications of the mortar element method. *GAMM-Mitt*, 28(2):97–123, 2005.

[8] Helmut J. Bohm. A short introduction to basic aspects of continuum micromechanics. Technical report, Vienna University of Technology, Vienna, Austria, 2008.

[9] S P A Bordas and Marc Duflot. Derivative recovery and \emph{a posteriori} error estimate for extended finite elements. *Computer Methods in Applied Mechanics and Engineering*, 196(35-36):3381–3399, 2007.

[10] B Boroomand and O C Zienkiewicz. An improved {REP} recovery and the effectivity robustness test. *International Journal for Numerical Methods in Engineering*, 40(17):3247–3277, 1997.

[11] Emanuela Bosco. *Computational homogenization formulations for localization and multiphysics phenomena in energy storage materials*. PhD thesis, Universita degli studi di Brescia, 2012.

[12] Markus J Buehler and Huajian Gao. Ultra large scale simulations of dynamic materials failure. In *Handbook of Theoretical and Computational Nanotechnology*, volume X, chapter 14, pages 1–41. 2005.

[13] E. W. C. Coenen, V. G. Kouznetsova, and M. G. D. Geers. Multi-scale continuous-discontinuous framework for computational–homogenization-localization. *Journal of the Mechanics and Physics of Solids*, 60(8):1486–1507, April 2012.

[14] M A Crisfield. Accelerated solution techniques and concrete cracking. *Computer Methods in Applied Mechanics and Engineering*, 33(1-3):585–607, 1982.

[15] M A Crisfield. *Non-linear finite element analysis of solids and structures: advanced topics*. John Wiley & Sons, Inc., New York, NY, USA, 1st edition, 1997.

[16] Hachmi B E N Dhia. Multiscale mechanical problems: the Arlequin method. *Comptes Rendus de l'Academie des Sciences Series IIB Mechanics Physics Astronomy*, 326(12):899–904, 1998.

[17] A Cemal Eringen. *nonlocal continuum field theories*. springer, 2001.

[18] Charbel Farhat and FX Francois-xavier Roux. A method of finite element tearing and interconnecting and its parallel solution algorithm. *International Journal for Numerical Methods in Engineering*, 32(6):1205–1227, 1991.

[19] Rixen D. Farhat C, Lacour C. Incorporation of linear multipoint constraints in substructure based iterative solvers. Part 1: a numerically scalable algorithm. *International Journal for Numerical Methods in Engineering*, 43(6):997– 1016, 1998.

[20] Frederic Feyel and Jean-louis Chaboche. FE 2 multiscale approach for modelling the elastoviscoplastic behaviour of long fibre SiC / Ti composite materials. *Computer Methods in Applied Mechanics and Engineering*, 183:309–330, 2000.

[21] M G D Geers. Enhanced solution control for physically and geometrically non-linear problems. Part Iâthe subplane control approach. *International Journal for Numerical Methods in Engineering*, 46(2):177–204, September 1999.

[22] M.G.D. Geers, V. G. Kouznetsova, and W. A. M. Brekelmans. Multi-scale computational homogenization: Trends and challenges. *Journal of Computational and Applied Mathematics*, 234(7):2175–2182, August 2010.

[23] A. Ghosh and P. Chaudhuri. Computational modeling of fracture in concrete using a meshfree meso-macro-multiscale method. *Computational Materials Science*, 69(2013):204–215, March 2013.

[24] S. Ghosh, J. Bai, and P. Raghavan. Concurrent multi-level model for damage evolution in microstructurally debonding composites. *Mechanics of Materials*, 39(3):241–266, March 2007.

[25] Somnath Ghosh, Kyunghoon Lee, and Prasanna Raghavan. A multi-level computational model for multi-scale damage analysis in composite and porous materials. *International Journal of Solids and Structures*, 38(14):2335–2385, 2001.

[26] I Gitman, H Askes, and L Sluys. Representative volume: Existence and size determination. *Engineering Fracture Mechanics*, 74(16):2518–2534, November 2007.

[27] P Guidault and T Belytschko. On the L 2 and the H 1 couplings for an overlapping domain decomposition method using Lagrange multipliers. *International Journal for Numerical Method in Engineering*, 70(October 2006):322–350, 2007.

[28] R Hill. Elastic properties of reinforced solids: some theoretical principles. *J. Mech. Phys. Solids*, 11:357–372, 1963.

[29] Andrea Hund and Ekkehard Ramm. Locality constraints within multiscale model for non-linear material behaviour. *International Journal for Numerical methods in Engineering*, 70(December):1613–1632, 2007.

[30] Adnan Ibrahimbegovic and Damijan Markovic. Strong coupling methods in multi-phase and multi-scale modeling of inelastic behavior of heterogeneous structures. *Computer Methods in Applied Mechanics and Enginnering*, 192:3089–3107, 2003.

[31] P Kerfriden, P Gosselet, S Adhikari, and S P A Bordas. Bridging proper orthogonal decomposition methods and augmented Newton Krylov algorithms : An adaptive model order reduction for highly nonlinear mechanical problems. *Computer Methods in Applied Mechanics and Engineering*, 200:850–866, 2011.

[32] P. Kerfriden, O. Goury, T. Rabczuk, and Stéphane P.A. Bordas. A partitioned model order reduction approach to rationalise computational expenses in nonlinear fracture mechanics. *Computer Methods in Applied Mechanics and Engineering*, 256:169–188, April 2013.

[33] Pierre Kerfriden, O Allix, and P Gosselet. A three-scale domain decomposition method for the 3D analysis of debonding in laminates. *Computational Mechanics*, 44(3):343–362, 2009.

[34] V. G. Kouznetsova, W a. M Brekelmans, and F P T Baaijens. An approach to micro-macro modeling of heterogeneous materials. *Computational Mechanics*, 27(1):37–48, January 2001.

[35] V. G. Kouznetsova, M. G. D. Geers, and W. a. M. Brekelmans. Multi-scale constitutive modelling of heterogeneous materials with a gradient-enhanced computational homogenization scheme. *International Journal for Numerical Methods in Engineering*, 54(8):1235–1260, July 2002.

[36] P Ladevèze and J G Simmonds. *Nonlinear computational structural mechanics: new approaches and non-incremental methods of calculation*. Mechanical engineering series. Springer, 1999.

[37] Fredrik Larsson and Kenneth Runesson. On two-scale adaptive FE analysis of micro-heterogeneous media with seamless scale-bridging. *Computer Methods in Applied Mechanics and Engineering*, 200(37-40):2662–2674, September 2011.

[38] Seung-Cheol Lee, Marinos N. Vouvakis, and Jin-Fa Lee. A non-overlapping domain decomposition method with non-matching grids for modeling large finite antenna arrays. *Journal of Computational Physics*, 203(1):1–21, February 2005.

[39] J Lemaitre and J L Chaboche. *Mechanics of Solid Materials*. Cambridge University Press, 1994.

[40] Pierre-Louis Lions. On the Schwarz alternating method. I. In *In First international symposium on domain decomposition methods for partial differential equations*, pages 1–42, 1988.

[41] O Lloberas-Valls, D J Rixen, A Simone, and L J Sluys. On micro-to-macro connections in domain decomposition multiscale methods. *Computer Methods in Applied Mechanics and Engineering*, 225-228:177–196, June 2012.

[42] E. Lorentz and P. Badel. A new path-following constraint for strain-softening finite element simulations. *International Journal for Numerical Methods in Engineering*, 60(2):499–526, May 2004.

[43] Jan Mandel. Balancing Domain Decomposition. *Communications in Numerical Methods and Engineering*, 241(March 1992):233–241, 1993.

[44] T J Massart, R H J Peerlings, and M G D Geers. Structural damage analysis of masonry walls using computational homogenization. *International Journal of Damage Mechanics*, 16(2):199–226, April 2007.

[45] Bashir-Ahmed Memon, Xiao-zu Su, Memon Bashir-ahmed, and S U Xiao-zu. Arc-length technique for nonlinear finite element analysis. *Journal of Zhejiang University. Science*, 5(5):618–628, May 2004.

[46] Alexander Menk and Stéphane P.a. Bordas. Crack growth calculations in solder joints based on microstructural phenomena with X-FEM. *Computational Materials Science*, 50(3):1145–1156, January 2011.

[47] J.C. Michel and P. Suquet. Nonuniform transformation field analysis. *International Journal of Solids and Structures*, 40(25):6937–6955, December 2003.

[48] J. Mosler and I. Scheider. A thermodynamically and variationally consistent class of damage-type cohesive models. *Journal of the Mechanics and Physics of Solids*, 59(8):1647–1668, August 2011.

[49] S. Nemat-Nasser and M. Hori. *Micromechanics: overall properties of heterogeneous materials*, volume 1. 2 edition, 1999.

[50] Vinh Phu Nguyen, Oriol Lloberas-Valls, Martijn Stroeven, Lambertus Johannes Sluys, Comput Methods, Appl Mech, Oriol Lloberas Valls, and Lambertus Johannes Sluys. On the existence of representative volumes for softening quasi-brittle materials A failure zone averaging scheme. *Computer Methods in Applied Mechanics and Engineering*, 200:1220–1236, November 2011.

[51] Vinh Phu Nguyen, Oriol Lloberas-valls, Martijn Stroeven, and Lambertus Johannes Sluys. Computational homogenization for multiscale crack modeling . Implementational and computational aspects. *International Journal for Numerical Methods in Engineering*, 89(2012):192–226, 2012.

[52] P Raghavan, S Li, and S Ghosh. Two scale response and damage modeling of composite materials. *Finite Elements in Analysis and Design*, 40:1619–1640, 2004.

[53] E Riks. the application of Newtons method to the problem of elastic stability. *Journal of Applied Mechanics*, 39:1060–1065, 1972.

[54] M Ruess, D Schillinger, Y Bazilevs, V Varduhn, and E Rank. Weakly enforced essential boundary conditions for NURBS-embedded and trimmed NURBS geometries on the basis of the finite cell method. *International Journal for Numerical Methods in Engineering*, 00:1–20, 2011.

[55] JCJ Schellekens and R De Borst. On the numerical integration of interface elements. *International Journal for Numerical Methods in Engineering*, 36:43–66, 1993.

[56] Z Shabir, E Van Der Giessen, C a Duarte, and A Simone. The role of cohesive properties on intergranular crack propagation in brittle polycrystals. *Modelling and Simulation in Materials Science and Engineering*, 19(3):1–21, April 2011.

[57] Pierre M. Suquet. Elements of homogenization for inelastic solid mechanics. In André Sanchez-Palencia, Enrique and Zaoui, editor, *Homogenization Techniques for Composite Media*, pages 193–198. Springer Berlin Heidelberg, 1987.

[58] Hossein Talebi, Mohammad Silani, Stephane P A Bordas, Pierre Kerfriden, and Timon Rabczuk. A computational library for multiscale modeling of material failure. *Computational Mechanics*, pages 1–25, 2013.

[59] . Temizer and P. Wriggers. An adaptive multiscale resolution strategy for the finite deformation analysis of microheterogeneous structures. *Computer Methods in Applied Mechanics and Engineering*, 200(37-40):2639–2661, September 2011.

[60] S Toro, P J Sánchez, A E Huespe, S M Giusti, P J Blanco, and R A Feijóo. A two-scale failure model for heterogeneous materials : numerical implementation based on the finite element method. *International Journal for Numerical Method in Engineering*, (October):313–351, 2013.

[61] Jörg F. Unger. An FE2-X1 approach for multiscale localization phenomena. *Journal of the Mechanics and Physics of Solids*, 61:928–948, January 2013.

[62] Jörg F. Unger and Stefan Eckardt. Multiscale modeling of concrete. *Archives of Computational Methods in Engineering*, 18(3):341–393, July 2011.

[63] Clemens V Verhoosel, Joris J C Remmers, and Miguel A Gutiérrez. A partition of unitybased multiscale approach for modelling fracture in piezoelectric ceramics. *International Journal for Numerical Methods in Engineering*, 82(8):966–994, 2010.

[64] Franck J. Vernerey and Mirmohammadreza Kabiri. An adaptive concurrent multiscale method for microstructured elastic solids. *Computer Methods in Applied Mechanics and Engineering*, 241-244:52–64, October 2012.

[65] Yuping Wang, Roberto Ballarini, and GJ Rodin. Crack-tip parameters in polycrystalline plates with soft grain boundaries. *Journal of engineering mechanics*, 134(January):100–109, 2008.

[66] G A Wempner. Discrete approximation related to nonlinear theories of solids. *International Journal of Solids and Structures*, 7:1581–1599, 1971.

[67] A A Yazdani, A Gakwaya, and G Dhatt. An improved superconvergent patch recovery technique for the axisymmetrical problems. *Computers & Structures*, 66(6):799–821, 1998.

[68] O C Zienkiewicz and J Z Zhu. A simple error estimator and adaptive procedure for practical engineering analysis. *International Journal for Numerical Methods in Engineering*, 24(2):337–357, 1987.

[69] O C Zienkiewicz and J Z Zhu. The superconvergent patch recovery and a posteriori error estimates. Part 2: Error estimates and adaptivity. *International Journal for Numerical Methods in Engineering*, 33(7):1365–1382, 1992.

[70] Tarek I Zohdi, J Tinsley Oden, and Gregory J Rodin. Hierarchical modeling of heterogeneous bodies. *Computer Methods in Applied Mechanics and Engineering*, 138(1-4):273–298, December 1996.